Lithos 323 (2018) 174–190

Contents lists available at ScienceDirect

Lithos

journal homepage: www.elsevier.com/locate/lithos

Mapping magnetic sources at the millimeter to micrometer scale in dunite and serpentinite by high-resolution magnetic microscopy

Zeudia Pastore [a,*], Suzanne A. McEnroe [a], Geertje W. ter Maat [a], Hirokuni Oda [b], Nathan S. Church [a], Patrizia Fumagalli [c]

[a] Norwegian University of Science and Technology (NTNU), Department of Geoscience and Petroleum, Trondheim, Norway
[b] Geological Survey of Japan, National Institute of Advanced Industrial Science and Technology (AIST), Tsukuba, Japan
[c] University of Milan, Department of Earth Sciences "Ardito Desio", Milan, Italy

ARTICLE INFO

Article history:
Received 19 March 2018
Accepted 12 September 2018
Available online 18 September 2018

Keywords:
Magnetic anomalies
Scanning magnetic microscopy
Serpentinization
Dunite
Forward and inverse modeling
Natural remanent magnetization

ABSTRACT

Rock samples can have wide range of magnetic properties depending on composition, amount of ferromagnetic minerals, grain sizes and microstructures. Here, we used scanning magnetic microscopy, a highly sensitive and high-resolution magnetometric technique to map remanent magnetic fields over a planar surface of a rock sample. The technique allows for the investigation of discrete magnetic mineral grains, or magnetic textures and structures with submillimeter scale resolution. Here, we present a case-study of magnetic scans of pristine and serpentinized dunite thin sections from the Reinfjord Ultramafic Complex, in northern Norway. The magnetic mineralogy is characterized by electron microprobe, scanning electron- and optical-microscopy, and with rock magnetic methods. In serpentinized samples the magnetic carrier is end-member magnetite occurring as large discrete grains and small grains in micron scale veins. By contrast, the pristine dunite sample contains large Cr-spinel grains with very fine equant exsolutions ranging in composition from ferrichromite to end-member magnetite. Forward and inverse modeling of the magnetic anomalies is used to determine the remanent magnetization directions and intensities of discrete magnetic sources observed in the scanning magnetic microscopy. The fine-scale magnetization of the rock sample is used to investigate the magnetic carriers and the effect of serpentinization on the magnetic properties of the dunite. Modeling shows that the dipolar magnetic anomalies that are mapped by scanning magnetic microscopy are caused by grains with heterogeneous magnetic sources. The intensity of the magnetization and the amount of magnetic minerals are higher in the serpentinized sample than the pristine dunite sample, consistent with the measured bulk magnetic properties. Furthermore, the serpentinized samples show a larger variability in the direction of the magnetization and a stronger heterogeneity with respect to the pristine sample. The ability to rigorously associate components of the bulk magnetic properties to individual mineral phases creates new possibilities for rock magnetic, paleomagnetic, and exploration applications.

1. Introduction and geological setting

Geological samples have a wide range of magnetic properties depending on quantity of ferromagnetic minerals, and their compositions, grain sizes and microstructures. These properties influence magnetic anomalies from the micro- to the planetary scale. The natural remanent magnetization (NRM) of a sample is additionally dependent on the time and conditions of magnetic acquisition, so it reflects and can record the geological history of the sample. Secondary processes such as serpentinization or metamorphism can significantly alter both mineralogical characteristics and NRM, dramatically affecting rock magnetic properties and in turn changing the nature of the magnetic anomalies. Therefore, a comprehensive characterization of the magnetic petrology of the rock and its thermal history is needed for accurate interpretation of magnetic anomalies.

Rock magnetic methods are widely applied to measure rocks magnetic properties and characterize the carriers. While indispensable, traditional methods are bulk measurements that do not directly relate magnetic properties to individual mineral phases or microstructures. To attribute specific magnetic signals to the underlying mineralogy, techniques must be employed that can resolve magnetic properties at a fine scale. The ability to discriminate differing behavior of constituent phases is necessary for a complete understanding of the origin of bulk behavior measured in both the laboratory and in magnetic surveys, and provides vital evidence about primary and secondary geological processes and their role in determining magnetic response. One such technique that offers spatially-resolved measurements of magnetic

* Corresponding author.
E-mail address: zeudia.pastore@ntnu.no (Z. Pastore).

https://doi.org/10.1016/j.lithos.2018.09.018
0024-4937/

signals is scanning magnetic microscopy (e.g. Fu et al., 2014; Fukuzawa et al., 2017; Hankard et al., 2009; Lima et al., 2014; Noguchi et al., 2017; Oda et al., 2011; Tominaga et al., 2017; Weiss et al., 2000; Weiss et al., 2007). This emerging technique generates an accurate map of the magnetic field distribution over a planar surface of a rock sample with submillimeter resolution. Previous applications of scanning magnetic microscopy have been primarily as an extension of, and complement to traditional paleointensity and paleomagnetic techniques. Weiss et al. (2008) used the technique to investigate fine scale heterogeneity of magnetization in Martian meteorites and estimate the ancient Martian field strength. Paleointensity estimates are commonly based on bulk measurements, and do not account for the non-unidirectional orientation of the fine scale magnetization of the sample, which controls the bulk properties. Tominaga et al. (2017) investigated changes in the magnetic field intensity with the mineralogy during a carbonation sequence and used scanning magnetic microscopy to trace the reaction front. Oda et al. (2011) and Noguchi et al. (2017) used SQUID magnetic microscopy to generate a fine scale magnetostratigraphy to estimate ages and growth rate of ferromanganese crust.

While scanning magnetic microscopy has been applied in Earth sciences for several decades (Thomas et al., 1992), interpretation of the data remains an unresolved problem. Most previous work modeled the data acquired by scanning magnetic microscopy in terms of dipole moment intensity and directions, which is sufficient for paleomagnetic and paleointensity studies and appropriate for sources with simple geometries. However, laterally extensive sources, or those with non-uniform magnetization, common in nature, may not be accurately described by single dipole field. Furthermore, comparison with bulk measurements requires that the volume of the magnetic material be taken into account, hence calculating magnetization, rather than moment. Weiss et al. (2002) describe an inversion method to calculate the magnetization distribution from magnetic scan data using a grid of evenly spaced dipoles, with a fixed volume for grid voxels. The size of the data sets, however, means that such methods are computationally intensive and time-consuming. Here, we propose an alternative approach to a full scan inversion, or to the dipole moment determination. This consists of forward modeling of the magnetization of a three-dimensional source geometry using the compositional and geometrical constraints given by optical and electron microscopy. This approach, by including the geometry of the source, limits the degrees of freedom which characterize the inherently non-unique magnetic data inversions. We propose forward modeling to estimate the magnetization of discrete sources. When applied to the entire sample, the magnetization estimates of discrete grains can then be compared to the bulk properties of the sample.

Here, scanning magnetic microscopy and forward magnetic modeling are used in combination with chemical and magnetic properties analyses to characterize the magnetic carriers in three samples; a pristine dunite sample (CS4), and two highly serpentinized samples (15S2D and 15S2B).

The samples are from the Reinfjord Ultramafic complex (RUC) (Fig. 1), of the Seiland igneous province (SIP) in northern Norway. This complex was emplaced during the Ediacaran at a depth of 25–35 km (Larsen et al., 2018) and later uplifted. The SIP is now exposed in the Middle Allochthon of the Norwegian Caledonian belt. Although the SIP has a complex geodynamic history, most of the magmatic textures of its rocks are well preserved. The samples were selected to examine the origin of the primary magnetization in the dunite, and the effect of later serpentinization on the bulk properties. The pristine samples are believed to preserve primary NRM carriers of the lower crust, a topic of debate that is strongly linked to the thermal history of the rocks (McEnroe et al., 2018). In addition, there are local serpentinized areas within the ultramafic outcrops. Serpentinization is a relatively low temperature (≤400 °C) fluid-mediated hydration process and in ultramafic rocks commonly leads to the production of magnetite. The creation of secondary magnetite could result in a composite NRM of the rock, a combination of the primary and secondary magnetizations, or may completely overprint the original NRM. The characterization of the NRM of discrete magnetite grains could be useful to distinguish different stages of serpentinization. By directly relating the micrometer scale anomalies to the mineralogy, we can improve our understanding of processes that control the magnetism of a rock and link

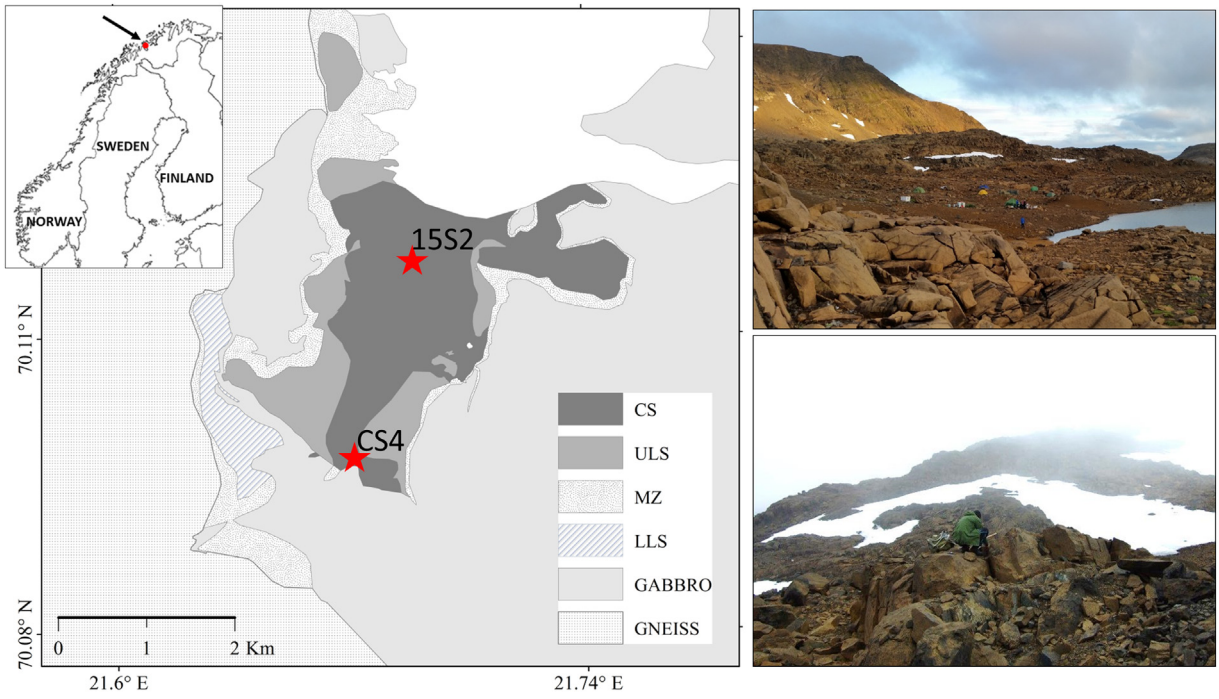

Fig. 1. Geological map of the Reinfjord Ultramafic Complex (modified after Grannes, 2016) with samples localities (red stars); CS4 sample is taken from the southern side of the complex, while the 15S2 locality is from the northern side. Right: outcrops photographs of the dunite rocks from the Central Series formation. The ultramafic complex, surrounded by gabbroic rocks and gneisses, consists of three ultramafic series: the Central series (CS), the upper layered series (ULS) and the lower layered series (LLS).

these to the geological history. A greater understanding of the processes and features at the mineral scale will enhance our interpretation of magnetic anomalies on outcrop, regional, and planetary scales.

2. Methods

We investigated three samples of the Reinfjord Ultramafic Complex with optical and electron microscopy, rock magnetic methods, and magnetic modeling. Microscopy provides precise measurements of size, shape, and chemical composition of oxide and sulphide particles in a thin section, which had been surveyed in the scanning magnetic microscope before exposure to electron microscope fields. Bulk magnetic properties were measured on chips or cores of companion samples. Magnetic modeling of the magnetic microscopy scans of the thin sections was applied to isolated anomalies associated with discrete grains to estimate the magnetization intensity and direction of the magnetic grains.

Modal mineralogy was investigated using optical and scanning electron microscopy (SEM) imaging by backscattered electrons at the NTNU NanoLab using a FEI Helios G4 UX scanning electron microscope (SEM). Chemical analyses were made using a JEOL 8200 SuperProbe (Electron Probe Microanalyzer-EPMA) at the University of Milan using wavelength-dispersive spectroscopy (WDS) techniques. All samples were analyzed at the microprobe with a spot current of 5 nA and 15 keV accelerating voltage. Points were spot analyzed with a beam diameter of 1 μm and measuring time of 10 s on background and 30 s on peak.

Thin-sections magnetic scans were made with a scanning SQUIDmicroscope at the Geological Survey of Japan, National Institute of Advanced Industrial Science and Technology (AIST), and on a newly built scanning magnetic tunnel junction instrument (here after referred to as the MTJ microscope) at the NTNURock- and Paleomagnetism laboratory. Both instruments measure the vertical component of the field and all imaging was carried out at room temperature (~20 °C) in field-free conditions. Therefore the signals represent remanent behavior. The nominal sampling step for all scans is 100 μm in x and y. The SQUID microscope system uses a 200 × 200 μm square washer type pickup coil, which has a field resolution of 1.1 pT/√Hz at 1 Hz (Kawai et al., 2016) and a sample stage with positioning accuracy of ~10 μm (Oda et al., 2016). Measurements were conducted with a sensor-to-sample distance of approximately 253 μm. The MTJ microscope hasfield noise of ~70 nT/√Hz at 1 Hz, and positioning accuracy of ~100 nm; the poorer noise performance of this instrument is partially offset by averaging 5 identical measurements. Asensor-to-sample distance of approximately 200 μm was used for the surveys with this instrument. The spatial resolution of discrete magnetic sources in both devices is dependent on the sensor active area, scanning step size, positioning accuracy, measurement speed, sensor-to-sample distance and on the thickness of the magnetization distribution. Modeling of the magnetic data acquired by magnetic scanning microscopy was made using Tensor Research ModelVision software.

Bulk rock magnetic property analyses were performed at NTNU using a variety of techniques. NRM was measured on sample cores of 2.5 cm diameter and 2.2 cm height, or sample chips using an AGICO JR6 spinner magnetometer with sensitivity of 2 μA/m. Susceptibility values were measured using a Sapphire susceptibility bridge on sample cores and an AGICOMFK1-A Kappabridge on sample chips with sensitivity of $6{\cdot}10^{-8}$ SI.

Temperature dependence of AC susceptibility was measured in argon, and in air using an AGICOMFK1-A-Kappabridge on powdered samples. For high temperature measurements, samples were heated from room temperature (RT) to 700 °C before cooling again to ambient temperature at an interval of 11 °C/min; for low temperature run, samples were cooled from room temperature to −194 °C and then heated back to room temperature.

High- and low-field susceptibility, saturation remanence (Mr) and saturation magnetization (Ms) curves were measured as a function of temperature using a Princeton PMC Model 3902/F MicroMag Vibrating Sample Magnetometer (VSM) with a flowing helium furnace instead. The instrument measures the magnetic moment with an average sensitivity of 0.5 nA· m^2. Measurements were made on chips of the samples using the quarter-hysteresis loop method of Fabian et al. (2013) here with a maximum field of 1 Tesla. Curie temperatures and blocking behavior were estimated from thermomagnetic curves. Room temperature hysteresis measurements were acquired before and after each thermal experiment.

3. Data and results

3.1. Petrography and mineral chemistry

The three RUC samples discussed here are a pristine dunite sample CS4, and two serpentinized dunite samples 15S2D and 15S2B. Samples contain minor opaque phases including oxides and sulfides (pentlandite, pyrrhotite and chalcopyrite). Accessory amounts of amphibole, pyroxenes, calcite, dolomite and biotite are also present.

Based on image analysis of optical images, mineral phases abundances of sample CS4 result is 92.3% olivine in large subhedral crystals (1–3 mm in size), 7% pyroxenes (diopside and enstatite), occurring as interstitial grains between olivine grains, and the remaining 0.7% opaque minerals, including oxides and sulfides. The dominant opaque mineral is Cr-spinel. Minor amounts of ilmenite and pentlandite are present. Opaque grain sizes are ≤0.1–1 mm. Backscattered electron (BSE) images of the Cr-spinel grains show these are not homogeneous and host fine-grained Fe-rich intergrowths (Fig. 2) with sizes varying from ≤200 nm to 5 μm. The Fe-rich exolution 'blebs' are all designated as ferrichromite; however there is a variation in Fe-rich compositions and some are near -or end-member magnetite.

In the heavily serpentinized samples (15S2D and 15S2B) olivine has been mostly replaced by lizardite, brucite and magnetite; however, some relict olivine and pyroxene grains are recognizable in cross-polarized light. Based on image analyses of optical images, sulfides and oxides constitute up to the 7% of the serpentinized samples. The sulfides are mostly pentlandite and pyrrhotite with minor chalcopyrite. The main oxides are magnetite, ilmenite and Cr-spinels. Backscattered electron (BSE) images of opaque minerals show that spinel grains from serpentinized samples are homogeneous, unlike the Cr-spinel grains in CS4. Magnetite is present throughout the thin section, in small few-micrometer-thick veins (Fig. 3g, h), or in large grains (up to 700 μm) together with pentlandite (Fig. 3), Al—Cr spinel and ilmenite (Fig. 3a, c, d).

Of the opaque grains, ferrichromite, magnetite and monoclinic pyrrhotite retain a remanent magnetization. Because the magnetic properties of these phases are strongly controlled by their composition, precise chemical analyses were measured. Measurements were taken from a homogeneous spot area at the microprobe scale. Analyses were calculated as weight percent of oxides. Representative analyses of spinels are shown in Table 1. Cations ratios are given per formula unit (p.f.u.).

The larger oxides grains in the pristine dunite sample (CS4) contain two phases (Fig. 2). The host grain consists of Cr- spinel with modal composition $(Fe^{2+}_{0.76}\ Mg_{0.25})_{1.01}(Fe^{3+}_{0.46}Cr_{0.74}Al_{0.75}Ti_{0.03})_{1.97}O_4$, while the exsolved phase is ferrichromite with modal composition $(Fe^{2+}_{0.94}\ Mg_{0.07}Ni_{0.01})_{1.02}(Fe^{3+}_{1.33}Cr_{0.46}Al_{0.15}Ti_{0.03})_{1.97}O_4$. Magnetite is the predominant Fe—Ti oxide in the serpentinized samples, and occurs in a wide range of grain sizes, varying from <1 μm to >400 μm. Cr-spinel is also present, however, it is more enriched in Al and Mg, and less enriched in Fe and Cr than in CS4, with modal composition $(Fe^{2+}_{0.53}\ Mg_{0.46})_{0.99}(Fe^{3+}_{0.15}Cr_{0.32}Al_{1.52})_{1.99}O_4$. The Cr-rich spinel grains in the serpentinized samples do not contain exolution microstructures observed in the dunite sample, CS4 (see Fig. 2).

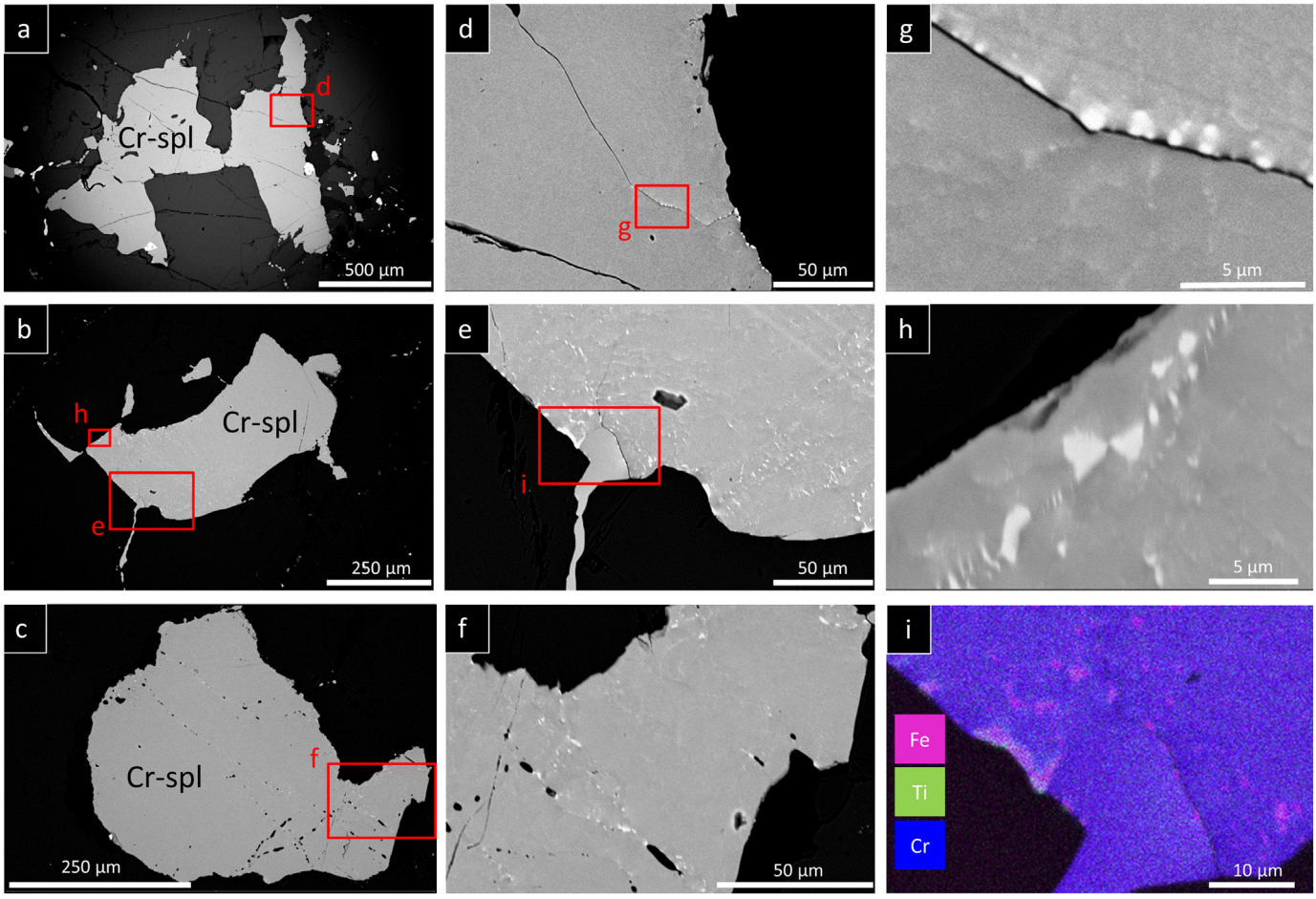

Fig. 2. SEM electron backscatter images from sample CS4(a-h) and element (Fe,Ti,Cr) map from EMP (i). a)Cr-spinel and (d, g)close up images on the same grain. Cr-spinel is in dark gray, and ferrichromite exolution blebs are light gray. b)Cr-spinel grain and (e, h)close up images on the same grain. Larger ferrichromite intergrowths occur on the margins at the contacts, or along fractures of the hosting grain. c)Cr-spinel grain and (f)close up images on the same grain. i)Elements map for selected area (red box in Fig.2e) showing ferrichromite (pink) and areas enriched in Ti, enclosed within a matrix of a Cr- and Al rich spinel (blue).

Spinel compositions from the dunite and serpentinite samples are shown on three plots in Fig. 4. In both dunite and serpentinized samples there is a bimodal distribution with a slight shift of the serpentinized samples' spinels (green symbols, Fig. 4a) towards higher Al content with respect to those from CS4 (pink) (Fig. 4a). Ti is present in only small amounts (0.0–0.33 p.f.u.); however spinels with higher Fe^{3+} content or Mg# in the range 5–12 (Fig. 4c), have more variable Ti content. A ternary plot of trivalent cations for the samples analyzed is shown in Fig. 4 and data are compared with the mafic and ultramafic spinel compositional fields from Barnes and Roeder (2001). The host and exsolved phases in the pristine dunite sample and the co-existing spinels in the serpentinite samples are separated due to the miscibility gap ("Spinel Gap" in Fig. 4a) in the solid solution. Data from our study plot along the three trends indicated as Cr—Al, Fe—Ti and Rum trends. According to Barnes and Roeder (2001) the Cr—Al trend is the result of equilibria between Al-bearing pyroxenes and Mg-rich spinels. Among the Fe-poor spinel grains, we observe a general enrichment in Al in spinels from the serpentinized sample with respect to those from the pristine dunite. This difference could be related to primary local heterogeneity in the melts, or to reaction of the primitive spinels with the silicates during later serpentinization. The formation of lizardite at the expense of diopside would cause an increased Al/Mg ratio in the fluid. The increased mobility of Fe, generally observed after serpentinization, can further favor iron oxide production and particularly the crystallization of magnetite (top corner in Fig. 4a and top right corner in Fig. 4b), the endpoint of the Fe—Ti trend. Barnes and Roeder (2001) attribute the Fe—Ti trend to either the evolution of spinel compositions during fractional crystallization of silicates with consequent increase of Fe/Mg ratio and Ti content of the melt (Fig. 4c), or to the exchange of Fe^{2+} and Mg between spinel and coexisting silicates. In Fig. 4a spinels from both the dunite and serpentinized samples plot along this trend and show variable Ti contents (Fig. 4c). The ferrichromite lamellae (pink squares), previously shown in Fig. 2 are hosted by the Fe-poor spinels. The CS4 spinels are well grouped and have similar composition with Mg# between 24 and 28. The spinels from the serpentinized sample have a larger Mg# range and slightly lower Ti content. These differences result in an overlap with the Rum trend. This trend describes an increase in Al at the expense of Cr with decreasing Fe^{3+}, and has been attributed to the reaction between cumulus spinel grains and intercumulus liquid (Barnes and Roeder, 2001). We do not exclude that during serpentinization primary spinels have incorporated Al at the expense of Fe^{3+}, which has been accommodated instead the newly formed iron oxides.

3.2. Scanning magnetic microscopy

The magnetic scans of pristine sample CS4 and serpentinized 15S2D were acquired with a scanning SQUID microscope at the Geological Survey of Japan (GSJ) (Oda et al., 2016). The third scan (15S2B, serpentinite) was made at the NTNU laboratory of rock magnetism and paleomagnetism using a scanning magnetic microscope equipped with a magnetic tunnel junction sensor (Church and McEnroe, 2018). The thickness of the thin sections is 30 µm.

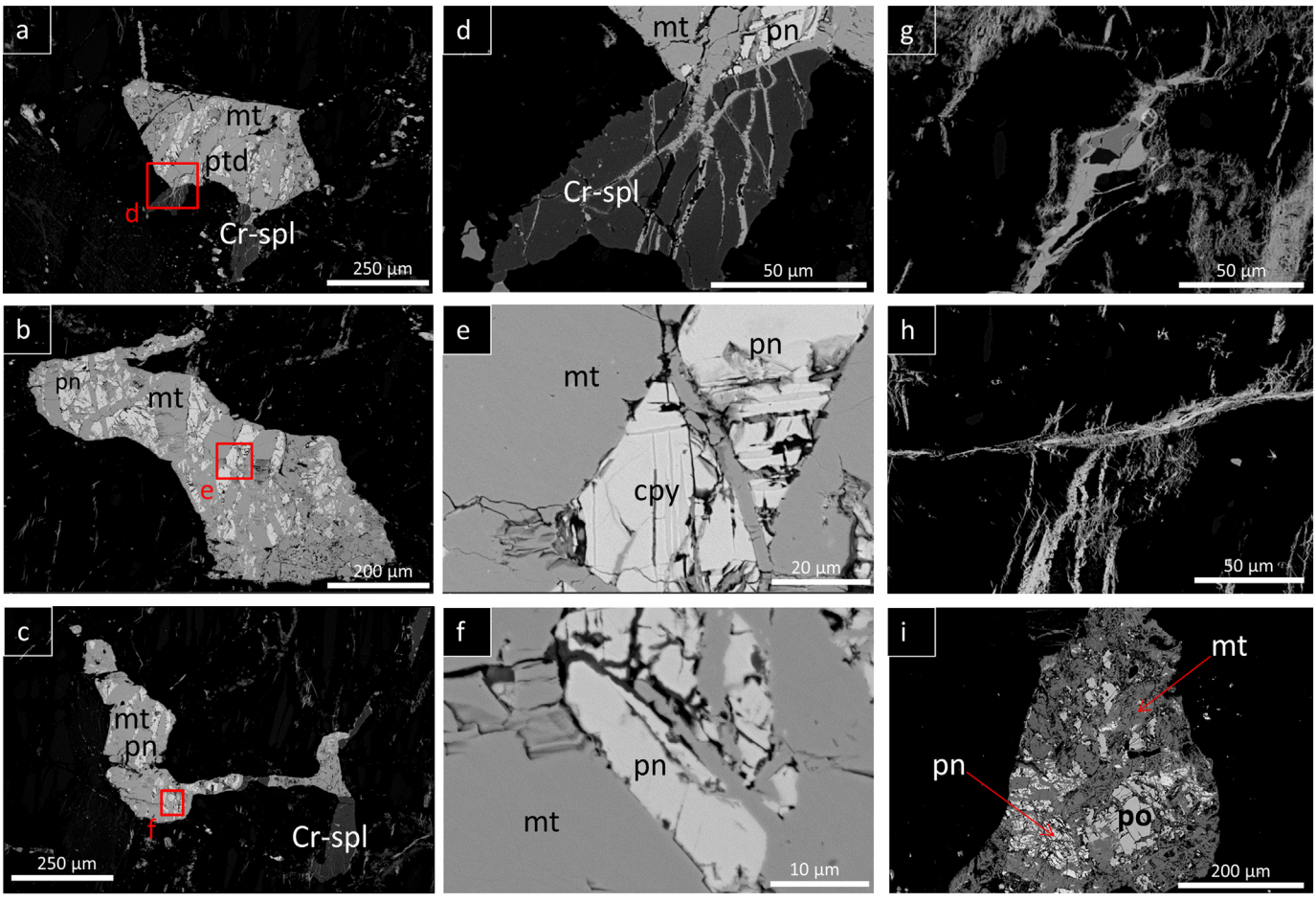

Fig. 3. SEM electron backscatter images from sample 15S2D. a)Magnetite (mt), pentlandite (pn) and Cr-spl assemblage and close up images on the grain (d). b)Magnetite, pentlandite assemblage and close up on the grain (e). c)Magnetite, pentlandite and Cr-spl assemblage and close up on the grain (f). g)Magnetite and Cr-spl in serpentine vein. h)Magnetite in vein. i)Magnetite (dark gray), pentlandite (light gray) and pyrrhotite (po) (medium gray) assemblage.

Aligned overlays of optical and magnetic scans of the thin sections are shown in Fig. 5. All scans measure the vertical component of the magnetic field and are shown on the same color scale. The measured field intensity ranges from −7500 nT to +8100 nT for CS4, from-2200 nT to +2300 nT for 15S2D and from −5000 to +9900 nT for 15S2B. In each scan several isolated magnetic anomalies related to discrete opaque mineralogy are observed.

In the dunite sample (CS4) the anomalies are commonly dipolar, in the plane of the sample, and oriented NE-SW(Fig. 5a). Slight variations in the directions are likely related to the shape and orientation of the grain. Most of the anomalies correlate with grains with an average surface of 300 µm*300 µm. With thin section thicknesses of 30 µm, this results in a high aspect ratio of the grains (≈10) which could influence the direction of magnetization. In 15S2D the anomalies are dipolar and in the plane of the sample, but are more randomly oriented compared to those in CS4. The amplitude of the anomalies is comparable, or lower than those observed in CS4. The 15S2B scan is dominated by three high-intensity anomalies that correlate with large (>200 µm diameter) grains of magnetite with pentlandite and chalcopyrite, two at the edge of the sample and one in the SE quadrant (Fig. 5c). Weaker and elongated anomalies are also present and correlate with the diffuse, fine magnetite in the serpentinized veins. The anomalies in the 15S2B thin section fall into two similar groups. The rounded, high intensity, in-plane signals are correlated with larger opaque grains and are similar to the stronger anomalies observed in 15S2D. The weaker, elongated anomalies correlate with the fine magnetite in serpentine veins. The two types of anomalies have two different directions, approximately 90° from each other (Fig. 5c) with the magnetite in the serpentine veins producing a signal approximately normal to the plane of the sample.

3.3. Rocks magnetic and physical properties

The concentration, composition, grain size, shape, and intergrowths or microstructures of magnetic minerals strongly control rock magnetic properties and particularly their ability to retain a stable magnetic memory over a geological time span (McEnroe et al., 2009a, 2009b; Robinson et al., 2016). Magnetically-ordered phases that possess spontaneous magnetization and are able to carry remanent magnetization are iron nickel alloys, uncommon in crustal rocks, or iron oxides and iron sulfides (monoclinic pyrrhotite). For the iron oxides in the chromite-magnetite solid solution the balance between Fe and Cr (or other cations) controls the magnetism of and affects intrinsic properties such as the Curie temperature (Robbins et al., 1971). Increasing substitution of cations such as Ti, Cr, Al and V in magnetite at the expense of Fe lowers the Curie temperature, although in whole-rock samples minor substitution does not necessarily produce weaker magnetic low-field susceptibility, or thermoremanent magnetization intensity, which in turn are more affected by grain size than composition (Clark, 1997). Here we investigated magnetic properties of the samples and estimate the Curie temperature, concentration, and grain size of the magnetic carriers using established magnetic methods, described below.

Table 1
Representative Wavelength-dispersive (WDS) chemical compositions of spinels in pristine dunite (CS4) and serpentinized (15S2D) samples. Values in parentheses correspond to 1σ standard deviation; n is the number of analyses. Detection limits ranges on analyzed elements are indicated for each group of analyses.

Sample	CS4				15S2D			
wt%	n = 5		n = 5		n = 6		n = 2	
TiO_2	0.97	(0.17)	1.81	(0.83)	0.01	(0.01)	0.10	(0.04)
Al_2O_3	20.22	(0.77)	2.79	(0.58)	0.00	(0.01)	45.63	(0.24)
Cr_2O_3	30.13	(1.70)	15.63	(1.43)	0.00	(0.01)	14.51	(0.11)
Fe_2O_3	16.79	(1.42)	48.11	(2.99)	70.25	(0.31)	7.37	(0.44)
FeO	27.39	(0.37)	31.37	(0.26)	31.53	(0.18)	22.38	(0.11)
MnO	0.28	(0.04)	0.21	(0.03)	0.03	(0.03)	0.17	(0.02)
MgO	5.64	(0.29)	1.31	(0.25)	0.02	(0.02)	11.09	(0.11)
NiO	0.08	(0.05)	0.21	(0.05)	0.08	(0.06)	0.23	(0.01)
Total	101.50		101.44		101.94		101.46	
Normalized to 3 Cations and 4 Oxygens								
Ti	0.023	(0.005)	0.050	(0.023)	0.000	(0.000)	0.002	(0.001)
Al	0.778	(0.026)	0.121	(0.025)	0.000	(0.000)	1.516	(0.010)
Cr	0.763	(0.040)	0.452	(0.040)	0.000	(0.000)	0.323	(0.002)
Fe^{3+}	0.412	(0.043)	1.325	(0.080)	1.996	(0.002)	0.156	(0.009)
Fe^{2+}	0.742	(0.016)	0.960	(0.013)	0.996	(0.003)	0.527	(0.003)
Mn	0.008	(0.001)	0.007	(0.001)	0.001	(0.001)	0.004	(0.001)
Mg	0.271	(0.014)	0.072	(0.013)	0.001	(0.001)	0.466	(0.004)
Ni	0.003	(0.001)	0.006	(0.001)	0.003	(0.002)	0.005	(0.000)
Total	3.000		2.993		2.997		2.999	
Detection limits ranges (ppm)								
Ti	310–353		331–367		343–407		291–320	
Al	143–162		141–153		141–155		170–173	
Cr	381–410		380–412		408–423		334–350	
Fe	373–399		413–457		450–468		351–351	
Mn	411–469		392–420		362–403		338–368	
Mg	136–178		132–158		118–153		169–167	
Ni	407–433		424–473		439–468		367–402	

3.3.1. Natural remanent magnetization, magnetic susceptibility and density

The samples show distinctly different bulk magnetic and density properties, due to the effect of serpentinization on diverse petrophysical parameters (Table 2). The NRM varies between 0.6 and 1.0 A/m in the pristine sample and between 2.7 and 6.9 A/m in the serpentinite. The magnetic susceptibilities of the serpentinite samples are 1–2 orders of magnitude higher than the dunite, consistent with the production of magnetite during serpentinization. Densities are significantly lower in the 15S2D and 15S2B cores (average density of 2.8 g/cm^3) with respect to the CS4 core (3.4 g/cm^3). Most of the primary olivine and pyroxenes in the serpentinized samples have been replaced by lizardite or brucite, which have a lower density.

3.3.2. Hysteresis parameters

Room temperature hysteresis behavior is primarily controlled by the magnetic mineralogy and the domain state. The characteristic quantities calculated from the hysteresis loop are saturation magnetization Ms, the remanent magnetization Mr, and the coercivity field Hc; the coercivity of remanence Hcr is measured using a separate remanence analysis. Table 2 summarizes hysteresis parameters for the samples, companion specimens were used for the high-temperature measurements and their properties are summarized in Table A1.

Ms is directly proportional to the magnetic content of the samples and is used to determine the volume magnetite content in the samples. This is estimated to be 2.5–3.0% in the serpentinized samples and 0.1% in the dunite. For the latter, 0.1% is a minimum estimate of the actual volume of ferromagnetic minerals within the sample, because the Ms of magnetite used in the calculation is higher than the Ms of cation-substituted compositions, in the magnetite-chromite solid solution. Therefore there could be slightly higher modal amount of ferromagnetic minerals. The electron microprobe analyses did not reveal endmember magnetite but rather ferrichromite with composition x = 1.4 in the

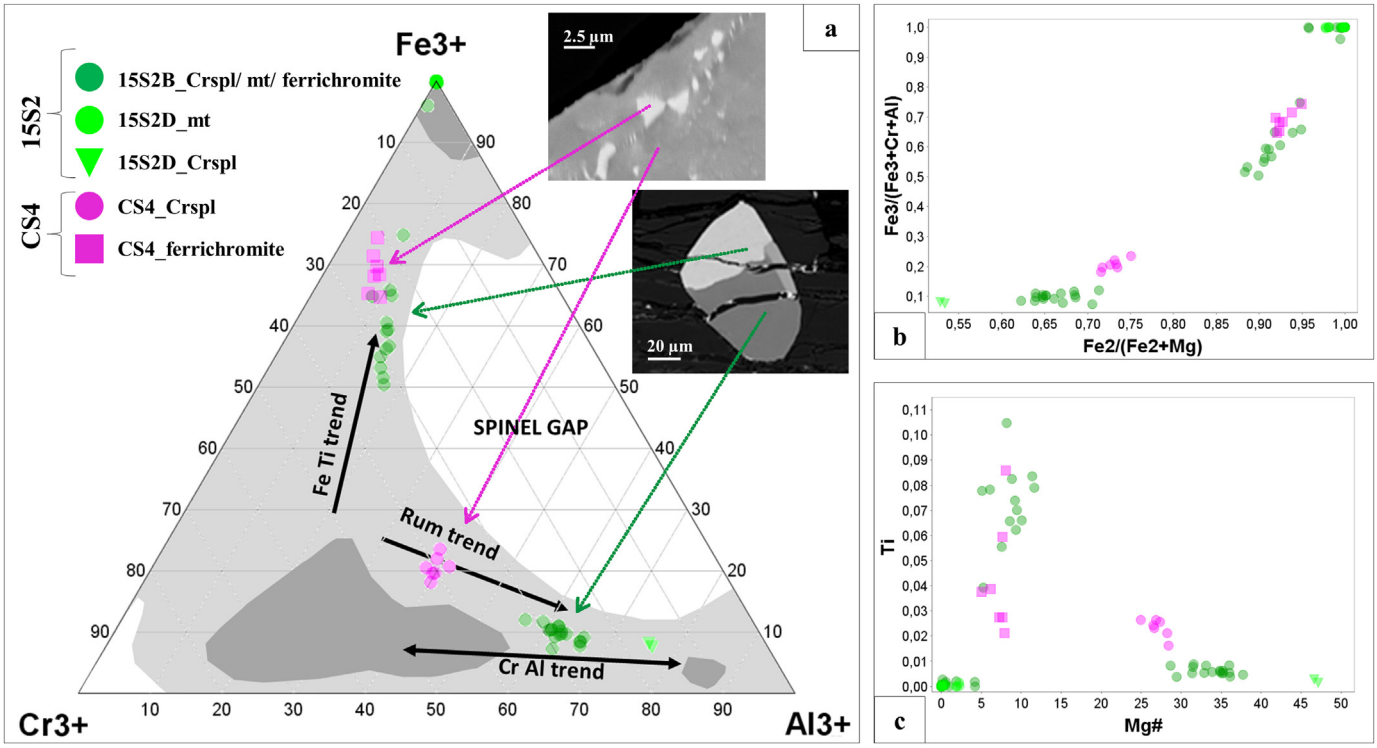

Fig. 4. Spinel compositional data for CS4 (pink) and 15S2 (green). a)Ternary plot of trivalent cations (atomic Cr3+, Fe3+, Al3+) with spinels compositional fields (different gray colors on the background are for different data concentrations) and trends (black arrows) from Barnes and Roeder (2001). Illustrative SEM backscatter images for spinels compositions from CS4 and 15S2 samples. (b)$Fe^{2+}/(Fe^{2+} + Mg)$ versus $Fe^{3+}/(Fe^{3+} + Cr + Al)$. d)Ti versus Mg# (Mg/(Mg + Fe^{2+})).

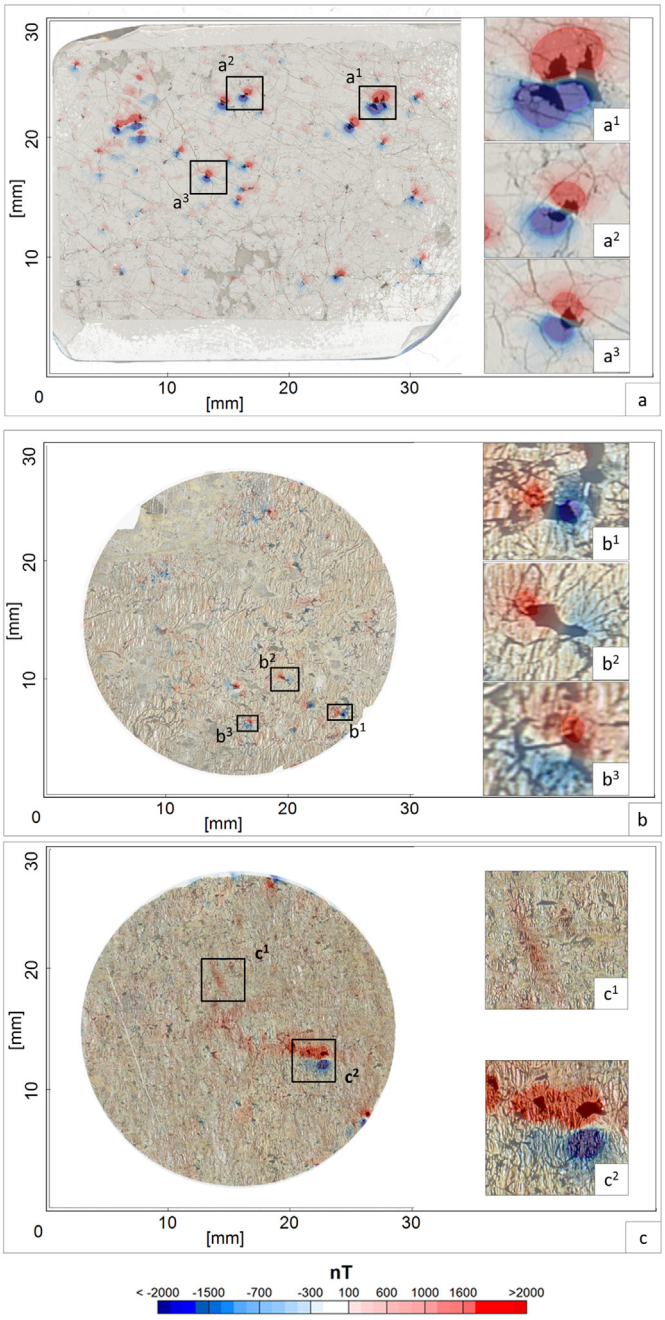

Fig. 5. Overlays of the magnetic anomaly maps with the optical scans for (a)CS4, (b)15S2D and (c)15S2B. Shown in insets to the right are enlarged views of selected anomalies. Figs. 2 and 3 show high-magnification SEM backscatter images of the same opaque grains causing the anomalies in a1, a2, a3 (CS4) and b1,b2,b3 (15S2D) respectively. All magnetic scans measure the vertical field and are displayed with the same color scale in nT.

system $Fe^{2+}Cr_{2-x}Fe^{3+}{}_xO_4$. Using this composition and corresponding Ms of 230,000 A/m (calculated from Robbins et al., 1971), the volume percent of magnetic oxides is approximately 0.2%, double that obtained considering Ms of endmember magnetite. The volume percentage ofmagnetite can alternatively be calculated as a function of low-field susceptibility, volume % Mgt = volume susceptibility (k)/0.00347, an empirical estimation (Clark, 1997; Puranen, 1989). Estimates of magnetite content using this method included in Table 2 are similar to those calculated from Ms. The susceptibility calculation yields lower estimates for the whole serpentinite cores, which are approximately 30× the size of the individual chip samples. The magnetite estimates from both methods (0.1–0.2% for dunite CS4, 2.4–3.0% for serpentinites 15S2D and 15S2B) have similar trends to the estimate made by image analysis of 0.7% opaque minerals in the dunite and 7.0% in the serpentinite. Because the image analysis measures all opaque grains, including those non-magnetic, it is expected to yield a higher estimate than the magnetic measurements, however on both cases the ratio between the dunite and serpentinite is approximately 10×.

3.3.3. Thermomagnetic behavior

The Curie point (Tc), is the temperature below which a magnetic ordering generates a net (spontaneous) magnetization and is a diagnostic tool for identification of magnetic minerals. Above this temperature thematerial is purely paramagnetic (Dunlop and Özdemir, 1997). End-member magnetite is a commonly occurring natural magnetic oxide and has a distinct Curie point at 580 °C. However within solid solution series, the Curie point temperature varies over a wide temperature range and can be used to constrain the mineral composition, or oxidation state (Fabian et al., 2013; Kądziałko-Hofmokl et al., 2008; Petersen and Bleil, 1982; Readman and O'Reilly, 1972). To measure the Curie temperature, samples are heated in a magnetic field and their susceptibility, or Ms is measured as a function of temperature. Below are the results of the thermomagnetic experiments.

3.3.3.1. Low field susceptibility. Sample chips of CS4 and 15S2 were powdered for high-temperature susceptibility measurements. Companion specimens were measured in air and argon, to check for reduction or oxidation during the heating processes on specimens (Fig. 6). Each plot shows a curve for heating and cooling. Low temperature measurements were made before and after heating the sample to high temperature as a further check for alteration that may have occurred. With the exception of the CS4 sample measurement in air (Fig. 6a, left), all other plots show that the susceptibility at room temperature is similar before and after heating. However, in both argon and air measurements, the comparison between the cooling and the heating curves suggests an alteration of the sample with a loss in susceptibility after the heating process. Serpentinized samples show well-defined Hopkinson peak both on heating and cooling at ~570 °C, near the Curie temperature of endmember magnetite. This peak, typical of magnetite and other magnetic materials, manifests as an increase in magnetic susceptibility between the blocking and the Curie temperatures and is often indicative of fine-grained particles. The heating branches show a "hump" centered at 370 °C in both specimens (Fig. 6 b,c) suggesting ferrichromite (Table 3). The lower temperature hump between 150 and 170 °C may be due to the λ-transition from antiferro- to a ferrimagnetic behavior in pyrrhotite (Minyuk et al., 2013). From optical and electron microscopy pyrrhotite is more abundant in the 15S2B sample with respect to 15S2D, consistent with the more pronounced excursions around 150°C in the latter sample. Horen et al. (2014) describe a similar hump as consequence of oxidation and destabilization of ferrichromite with a mechanism of dynamic segregation (Domenichini et al., 2002). This mechanism describes the formation of a new low-temperature magnetic phase and destruction/rehomogenization of the material within the same heating cycle. This rehomogenization would explain the irreversibility of the thermomagnetic curve that shows only magnetite in the cooling curve (Fig. 6 b, c). Dehydration and/or reduction of hydroxides may also cause variations in the susceptibility (Funaki et al., 2000) and the irreversibility of the chemical reaction is consistent with the absence of these variations after heating.

The dunite sample (CS4) shows smooth heating and cooling curves, concave down, with no Hopkinson peak. The maximum susceptibility is reached around 240 °C for runs carried out in argon, and 190 °C for those in air. While the steepest descent in both measurements occurs at 560°C, indicating abundant, impure but near-endmember magnetite, the steady decline in susceptibility from ~240 °C is interpreted as a wide range of Curie temperatures, and hence, compositional variations. The heating and cooling curves are reversible when measured in argon atmosphere, indicating little change in the magnetic mineralogy during

Table 2
Samples densities and magnetic properties (left side of the table), and hysteresis measurements on chips of the samples (right side of the table). Volume percent magnetite is calculated by dividing the magnetic susceptibility (k)by 0.0347 (Clark, 1997) and is calculated from saturation moment by dividing the Ms of the sample by the product of Ms of pure magnetite (480,000 A/m), sample mass and sample density. The Königsberger ratio (Q)is the ratio between NRM and induced magnetization which is calculated multiplying the susceptibility and the local magnetic field (43.0012 A/m). The precision used in the table is significant.

Sample			Density [g/cm^3]	Susceptibility [SI]	NRM [A/m]	Q	Volume % magnetite from susceptibility	Chip Mass [g]	Mr [Am^2/kg]	NRM/Mr [%]	Ms [Am^2/kg]	Hc	Hcr	Mr/Ms	Hcr/Hc	Volume % magnetite from Ms
CS4	C1	Chip	3.3	0.006	0.7	2.6	0.2	2.73	0.03	0.75	0.12	16.3	37.4	0.22	2.30	0.1
	C2	Chip	3.4	0.006	0.8	3.0	0.2	0.98	0.03	0.89	0.14	13.9	35.9	0.18	2.58	0.1
	C3	Chip	3.3	0.007	1.0	3.1	0.2	0.40	0.03	0.90	0.16	13.5	35.0	0.20	2.60	0.1
	CS4	Core	3.4	0.005	0.6	3.1	0.1									
15S2	D1	Chip	2.8	0.089	5.4	1.4	2.6	0.53	2.01	0.10	4.89	30.2	41.7	0.41	1.38	2.8
	D2	Chip	2.6	0.101	5.0	1.2	2.9	0.82	2.14	0.09	5.55	29.7	41.5	0.39	1.40	3.0
	D3	Chip	2.7	0.085	4.7	1.3	2.5	0.86	1.58	0.11	4.40	31.2	45.7	0.36	1.47	2.5
	D	Core	2.8	0.048	4.8	2.3	1.4									
	B1	Chip	2.5	0.083	5.9	1.7	2.4	1.31	5.07	0.05	12.68	29.4	41.9	0.40	1.42	2.7
	B2	Chip	2.6	0.067	2.7	0.9	1.9	0.37	1.56	0.06	5.44	27.3	38.0	0.29	1.39	3.0
	B	Core	2.8	0.049	6.9	3.2	1.4									

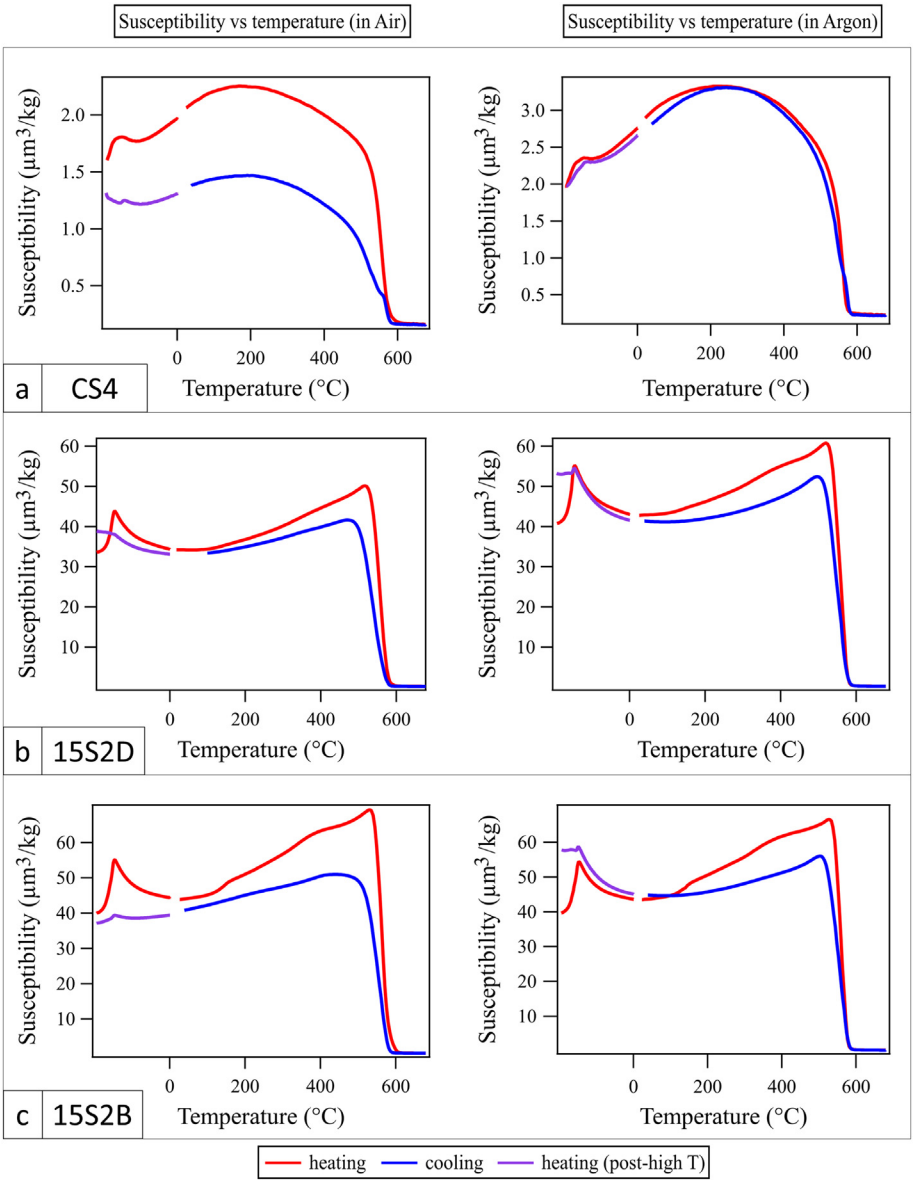

Fig. 6. Temperature dependent susceptibility curves in air (to the left) and argon (to the right) for CS4 (a), 15S2D (b), and 15S2B (c)samples chips. Susceptibility is normalized by the mass of the specimen.

Table 3
Tc estimates from representative oxides compositions, determined considering magnetite-spinel (Harrison and Putnis, 1996), magnetite-chromite (MC) (Francombe, 1957; Robbins etal., 1971) solid solution series and an interpolation between the two solid solution series. Chemical formulas do not account for elements with <0.01 p.f.u. Pm in the table indicates that the corresponding composition is paramagnetic at all temperatures.

Sample	Spinel Composition	Tc (°C) from composition		
		(Francombe, 1957; Robbins etal. (1971)	(Harrison and Putnis, 1996)	(Considering a combination of the M-C and M-S solid solutions)
CS4	$(Fe^{2+}_{0.76}\ Mg_{0.25})_{1.01}\ (Fe^{3+}_{0.46}\ Cr_{0.74}\ Al_{0.75}Ti_{0.03})_{1.97}\ O_4$ SPINEL/HERCYNITE	−120	−33	−90
	$(Fe^{2+}_{0.94}\ Mg_{0.07}\ Ni_{0.01})_{1.02}\ (Fe^{3+}_{1.33}\ Cr_{0.46}\ Al_{0.15}\ Ti_{0.03})_{1.97}\ O_4$ FERRICHROMITE	400	417	345
15S2D	$(Fe^{2+}_{0.53}\ Mg_{0.46})_{0.99}\ (Fe^{3+}_{0.15}\ Cr_{0.32}\ Al_{1.52})_{1.99}\ O_4$ SPINEL/HERCYNITE	−180	*pm*	−180
	$(Fe^{2+}_{0.98}\ Fe^{3+}_{2})_{2.98}\ O_4$ MAGNETITE (LARGE GRAINS)	585	586	580
	$(Fe^{2+}_{1}\ Mg_{0.02})_{1.02}\ (Fe^{3+}_{1.92})_{1.92}\ O_4$ MAGNETITE (VEIN)	580	583	580
15S2B	$(Fe^{2+}_{0.71}\ Mg_{0.29})_{1.00}\ (Fe^{3+}_{0.24}\ Cr_{0.62}\ Al_{1.11})_{1.97}\ O_4$ SPINEL/HERCYNITE	−150	−185	−125
	$(Fe^{2+}_{0.93}\ Mg_{0.12})_{1.05}\ (Fe^{3+}_{0.94}\ Cr_{0.57}\ Al_{0.30}\ Ti_{0.08}\ V_{0.02}\ Mn_{0.01})_{1.92}\ O_4$ FERRICHROMITE	205	276	196
	$(Fe^{2+}_{0.97}\ Mg_{0.05})_{1.02}\ (Fe^{3+}_{1.42}\ Cr_{0.33}\ Al_{0.15}Ti_{0.04}\ V_{0.01})_{1.92}\ O_4$ FERRICHROMITE	440	455	414
	$(Fe^{2+}_{0.99}\ Fe^{3+}_{1.98})_{2.97}\ O_4$ MAGNETITE	585	585	580
	$(Fe^{2+}_{1}\ Fe^{3+}_{2})_3\ O_4$ MAGNETITE (LARGE GRAINS)	585	586	580

heating. However, there is clear evidence for mineralogical change during the run in air, as indicated by the irreversibility of the thermomagnetic curves (Fig. 6a). On the cooling run, this sample exhibits a small inflection near 520 °C, below the highest Curie temperature. This second Curie temperature suggests a new phase was created during the experiment, possibly due to cation diffusion between the Fe-poor and Fe-rich regions of the Cr-spinel or the onset of spinodal decomposition.

All samples exhibit the Verwey transition, an abrupt excursion in magnetic susceptibility near −153 °C (120 K, Walz, 2002, and references therein), which is diagnostic of endmember magnetite. The transition in the pristine dunite is less sharp and begins at a lower temperature than the literature value, suggesting that magnetite has some small degree of cation substitution or non-stoichiometry. By contrast, the Verwey transition in the serpentinite samples (measured before heating) is sharp, indicating a near-endmember composition. Curie temperature estimates (Tc), based on representative composition of the magnetic mineralogy estimated from EMP data and on temperature dependent susceptibility curves, are listed in Tables 3 and 4, respectively. For the Tc estimates based on composition data we considered magnetite-spinel $(Fe_3O_4)_x\ (MgAl_2O_4)_{1-x}$ with $0 \le x \le 1$ and magnetite-chromite $Fe_{3-x}Cr_xO_4 0 \le x \le 2$ solid solution series (Table 3). For the magnetite-spinel solid solution series we refer to Harrison and Putnis (1996) where the Tc varies as a function of the mole fraction of magnetite (x)approximated by: Tc (°C) $= -853 + 2410\times - 970 \times {}^2$. For the magnetite-chromite solid solution series we refer to the combined data sets of Francombe (1957) and Robbins et al. (1971) fit with a logistic function. For comparison Tc estimates based on an interpolation between the two solid solution series are listed in Table 3. In both dunite and serpentinized samples the Fe-poor spinel compositions are paramagnetic at room temperature. Tc estimates for the ferrichromite vary between 200 °C and 400 °C depending on the cation ratios. To estimate Tc from the initial susceptibility, we used a derivative method that uses the maximum negative slope in the thermomagnetic curve (Table 4). For the serpentinized samples these Tc estimates on the heating curves are in the temperature range of 557–565 °C, whereas the cooling curves show Tc estimates in the range 520 °C–572 °C. This variability may indicate that some non-stoichiometric, non-endmember magnetite is present and that paramagnetic elements such as Al, Ti, Cr and/or Mg are substituted in the crystal lattice (Dunlop and Özdemir, 1997), to a greater extent in the dunite than in the serpentinite.

Table 4
Tc estimates from thermal experiments. Tc estimates based on high temperature measurements are determined from susceptibility (k)and Ms versus temperature curves using the derivative method described in the text. Blocking temperatures (Tb) are derived from Mr. Some samples have multiple Tc estimates in the cooling curve, which reflect the inception of spinodal decomposition during the experiment.

Sample	High-T experiment	Tc (°C) from k		Tc (°C) _Ms	Tb (°C) _Mr
		Heating	Cooling		
CS4	KB air	556	520		
			568		
	KB Ar	560	545		
			572		
	VSM	579		576	560
		574			
15S2D	KB air	557	541		
	KB Ar	559	542		
			561		
	VSM			567	150
					561
				565	156
					555
15S2B	KB air	565	562		
	KB Ar	148	544		
		561			
	VSM			576	153
					567

3.3.3.2. High temperature VSM measurements. An alternative calculation of the Curie temperature and a method to observe the evolution of other informative metrics as a function of temperature is provided by high-temperatureVSM measurements. The advantage of the VSM is that one measures four parameters (Ms, Mr and low- and high-field susceptibility). In strong-field measurements, the variation of the saturation magnetization with temperature is rigorous and more accurate indicator for the Curie temperatures than initial susceptibility and for the identification of ferro-, ferri- and antiferromagnetic states (Fabian et al., 2013; McEnroe et al., 2016).

High-temperature curves of Ms, Mr, high-field (χHF), and low-field (χ0) susceptibility are shown in Fig. 7 for samples CS4 (a-c), 15S2D (d-f) and 15S2B (g-i) chips. Temperature-dependent initial susceptibility (Fig. 7 a, d and g)curves are comparable to those measured on the Kappabridge (Fig. 6), albeit measured with different protocols. Sample CS4 shows a gradual decrease in initial susceptibility followed by a rapid decrease in the temperature range 560–580 °C. By contrast the serpentinized samples (15S2D and 15S2B) show an initial increase in susceptibility followed by a rapid decrease close to the Tc of magnetite.

The thermal curves of Mr and Ms are similar in both the 15S2D and 15S2B samples; Ms and Mr slowly decrease with temperature up to 530 °C and at a faster rate above this temperature. The point of maximum descent in Ms is a widely-applied technique for estimating the Curie temperature (Tauxe, 1998), though yields a slight underestimation (Fabian et al., 2013), and can be compared to similar calculations from low-field susceptibility measurements in the Kappabridge. Tc estimates based on Ms and unblocking temperatures from Mr are summarized in Table 4. In all samples, the Tc estimated from Ms is higher than that

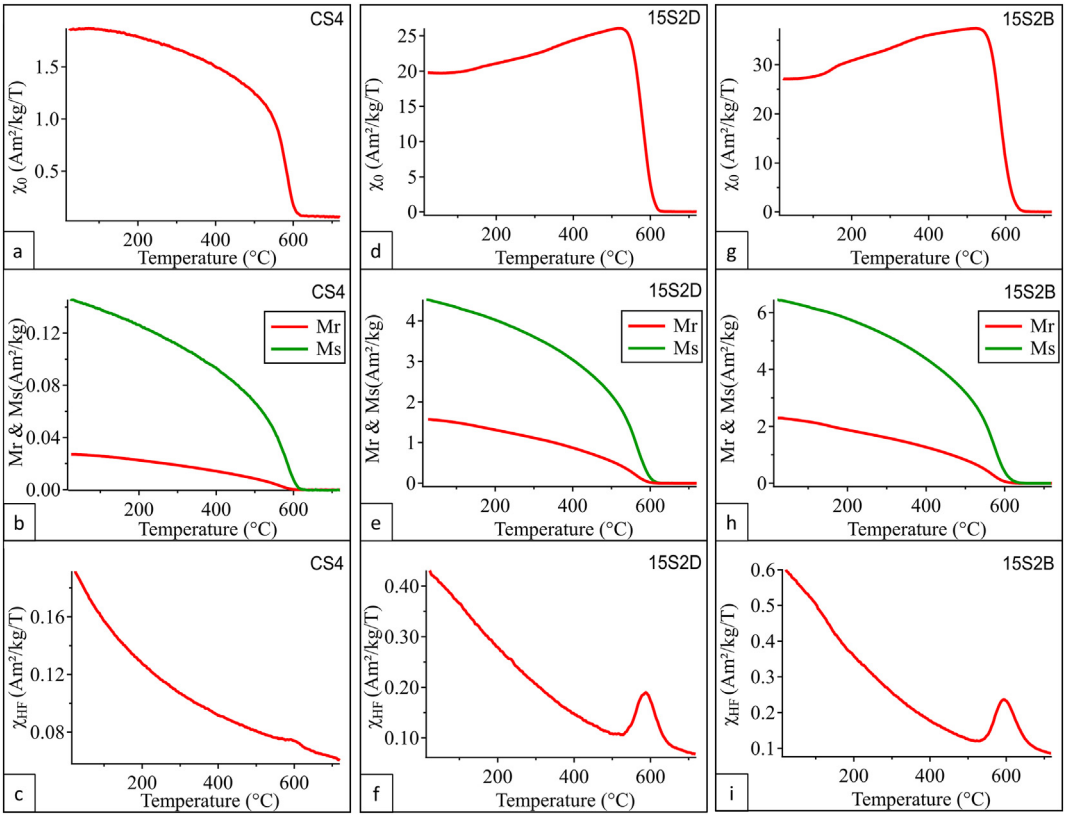

Fig. 7. High temperature experiments on 15S2 (15S2D and 15S2B) and CS4 samples chips. (a, d, g)Low-field susceptibility (χ0) versus temperature. (b, e, h)Mr and Ms versus temperature. (c, f, i)High-field susceptibility (χHF) versus temperature.

estimated from Kappabridge measurements, to a small degree in sample 15S2D and to a larger extent in CS4 and 15S2B. The Mr curves provide unblocking temperatures, the temperature above which particles have a spontaneous magnetization but due to thermal activation at high temperatures do not carry a stable remanence. The serpentinized samples demonstrate weak unblocking behaviour (with consequent loss of remanent magnetization) near 150 °C. At this temperature there is also a weak enhancement in susceptibility measured in both

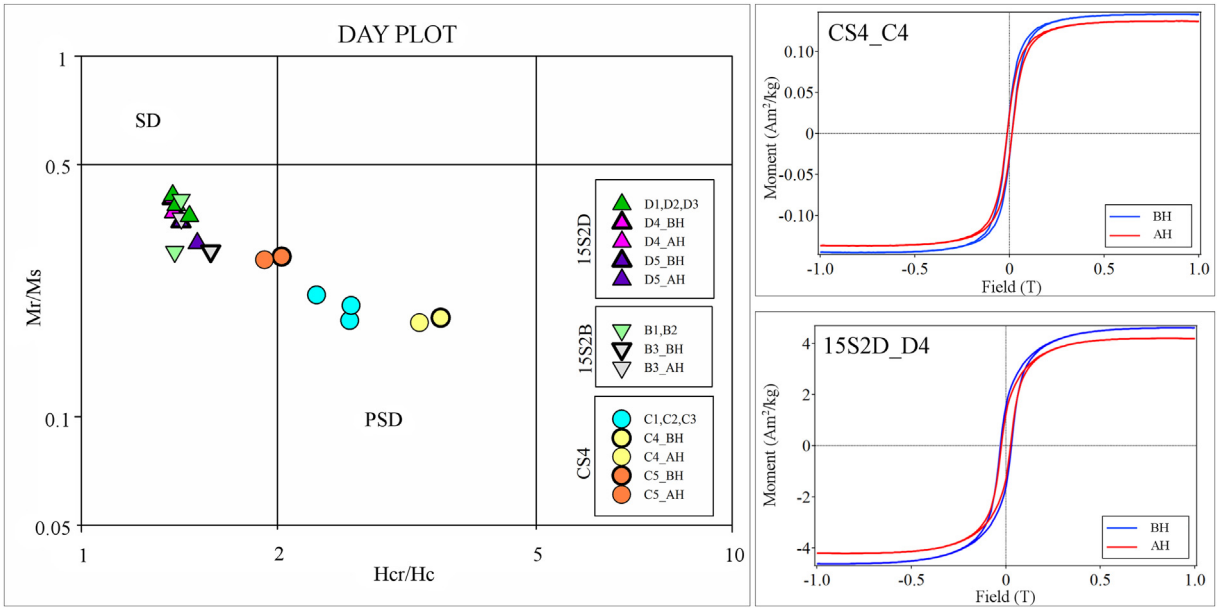

Fig. 8. Left: Day plot of Mr/Ms versus Hcr/Hc for specimens from the serpentinized samples (15S2D and 15S2B) and the pristine dunite sample (CS4) (after Day etal., 1977; Dunlop, 2002). CS4 sample plots in the pseudo-single domain (PSD) region while 15S2 samples plot closer to the single-domain (SD) region. These parameters are listed in Table 2 and Table A1. BH is before and AH after heating. Right: BH (blue) and AH (red) hysteresis loops for CS4_C4 (top) and 15S2D_D4 (bottom).

Kappabridge (Fig. 6) and VSM(Fig. 7) in sample 15S2B. The high-field (HF) susceptibility curve for 15S2 samples shows a clear Landau peak, slightly above Curie temperature for magnetite indicating ferrimagnetic ordering. These temperatures of 588 °C for sample 15S2D, and 595 °C for sample 15S2B, are higher than determinations from Ms, Mr or initial susceptibility, in agreement with Landau theory (Fabian et al., 2013). The Landau peak is visible, though small in the CS4 high-field susceptibility curve.

Room temperature hysteresis measurements were acquired before and after each thermal experiment, to characterize the sample, and to check for alteration that may have occurred during the heating. Representative hysteresis loops, measured before and after the high-temperatureVSM experiment are shown in Fig. 8. Hysteresis loops have been corrected for the paramagnetic contribution to isolate the ferromagnetic response. Both loops show a decrease in Ms after the high-temperature measurement, indicating some limited mineralogical change. Comparing the loops before heating, serpentinite sample 15S2D has a wider hysteresis loop than that of the pristine dunite CS4. The wider loop indicates a higher coercivity (Hc) in the serpentinized samples likely related to the presence of fine-grained magnetite, such as that observed in the veins.

Magnetic behavior, particularly remanence, is strongly influenced by magnetic domain state, which for magnetite can be estimated on the Day plot (Day et al., 1977). The Mr/Ms and Hcr/Hc ratios before and after heating are shown in Fig. 8, with additional measurements of other chips not used for thermomagnetic measurements, and limits of single-domain and pseudo-single domain behavior calculated by Dunlop (2002). The serpentinized samples cluster at high Mr/Ms and low Hcr/Hc values, approaching ideal single-domain behavior. By contrast, the pristine CS4 samples lie outside this cluster with parameters that generally fall within the pseudo-single domain region, which implies that at least some magnetic particles that contribute to the bulk properties are larger than single-domain. After the high temperature experiments the values of Ms, Mr, Hc and Hcr decrease slightly, indicating a change in chemical composition, grain size, and/or shape. This change is visible in the hysteresis loops and leads to slight shifts in the before-(BH) and after-heating (AH) positions of samples on the Day plot.

3.4. Magnetic data modeling

Scanning magnetic microscopy provides high resolution mapping of magnetic fields above the thin sections. The technique measures the vertical component of the magnetic field in field-free condition originating from the sample NRM. The measurements, made at room temperature can be correlated with the bulk magnetic properties of the sample. The magnetic field varies across the study thin sections, and is used to locate the magnetic carriers. These were investigated in both magnetic properties and mineral chemistry. The pristine dunite sample has distinctly different NRM intensity and susceptibility values than the serpentinized samples (Table 2). Here, we used magnetic modeling of these anomalies to characterize NRM directions and intensity of selected discrete grains.

3.4.1. Magnetic data and processing

Isolated magnetic anomalies are observed in all magnetic scans (Fig. 5) associated with the opaque mineralogy. Here we model three grains, one for each thin section, which correlate with strong dipolar anomalies (Fig. 9a, b and c). For each grain the magnetic anomaly and analytic signal maps are compared and shown overlaying the optical scan in Fig. 9. The analytic signal of the magnetic field was calculated to locate and distinguish among multiple sources contributing to each dipolar anomaly. This field transformation, obtained through a combination of the horizontal and vertical gradients of the magnetic field, does not depend on the direction of magnetization of the anomaly source, but depends on its location and shape. Assuming a rectangular, or Cartesian, coordinate system with the top plane of the thin section in the xy-plane and with the z-axis (measurement direction) perpendicular to it and directed downward into the thin section, we calculated the analytic signal of the vertical magnetic field (Bz). The amplitude of the analytic signal at (x,y) is calculated as the square root of the sum of the squares of the derivatives in the x, y, and z directions of the magnetic field Bz according to (Roest et al., 1992):

$$|AS(x,y)| = \sqrt{\left(\frac{\partial Bz}{\partial x}\right)^2 + \left(\frac{\partial Bz}{\partial y}\right)^2 + \left(\frac{\partial Bz}{\partial z}\right)^2} \quad (1)$$

Considering the high aspect ratio of our modeled grains, the analytic signal amplitude should have a maximum centered above the magnetic source (Nabighian, 1972). A comparison between the analytic signal and grain shapes shows that:

- For the grain in Fig. 9d, the analytic signal reflects the shape of the left side of the grain and indicates that region as the main source of the magnetic anomaly.
- For the grain in Fig. 9e, the analytic signal is dominantly centered over the grain with smaller highs towards the left side of the grain that could reflect compositional variations.
- For the grain in Fig. 9f, there are three different highs in the analytic signal, which can be distinguished, two correlating with large opaque grains, and one below one of the large grains. This may indicate an additional source of fine magnetite within the serpentinized veins.

3.4.2. Remanent magnetization modeling and results

We modeled the NRM intensity and direction of the three grains shown in Fig. 9, using a forward modeling approach with Model Vision. Modeling of each grain was made using homogeneously magnetized 3D frustum bodies with top and bottom constrained to be horizontal and defined by polygons, or tabular bodies with a maximum thickness of 30 μm (thin section thickness). Each body was then inverted for magnetization intensity and direction to obtain the best fit between observed and calculated anomaly field. Several tests weremade on selected grains. The best fitting models, for each test, are shown in Figs.10, 11 and 12, with their respective modeling parameters.

Modeling tests for a Cr-spinel grain from CS4 (Figs.2a & 5a) are shown in Fig. 10. Three different tests have been run (M1, M2 and M3). The first test considers a single large homogeneously magnetized grain, whose shape is constrained by the SEM images and by the thin section thickness of 30 μm. Inversions for magnetization intensities and direction gave a percentage root mean square error (RMS) of 9.2 for the best fitting model (M1). The RMS is expressed as a percentage of the dynamic range of the active data. It is calculated, for all positions at which the field values are used in the inversion, as the root mean square difference between the model input and output field values at a specific point, divided by the total range of the input magnetic field data in the modeled area. The second test was made using two sub-grains with same magnetization intensities and direction as in the M1 model, and inverting only for vertical extents of the two sub-grains and limiting this extent to a maximum of 30 μm. This test gave a lower RMS error of 6.6; the best fitting model M2 requires a lower thickness for the sub-grain to the right of the larger grain. The third test was made assuming three sub-grains of fixed thickness (30 μm) and freely variable magnetization intensity and directions. The best fitting model gave a RMS error to the observed anomaly of 4.1 and suggests a variable intensity of the remanent magnetization within the modeled grain, but broadly similar magnetization directions. For the magnetite grain with an intergrowth of pentlandite from 15S2D (Fig. 5b) three modeling tests were run and the best fitting models are shown in Fig. 11. Model M1 assume a homogeneously magnetized grain and gave a RMS error of 13. In model M2 the grain is subdivided in three smaller grains with

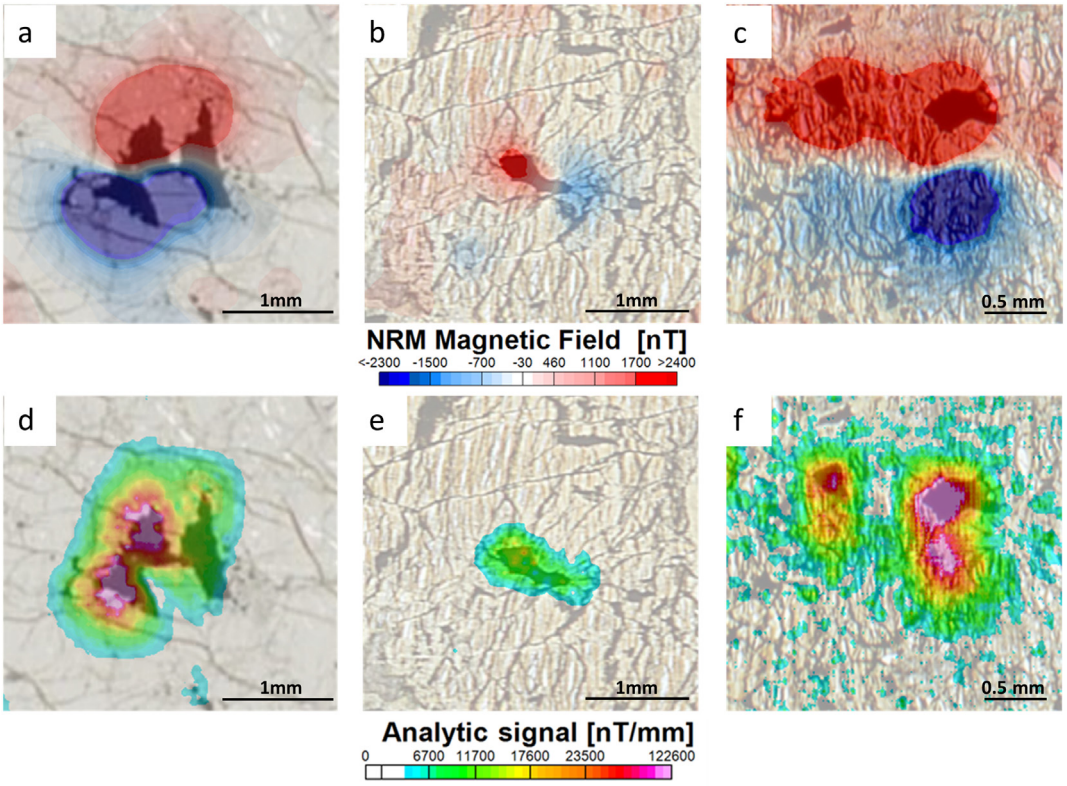

Fig. 9. Magnetic anomaly maps (top) and analytic signal maps (bottom) for three selected grains. Displayed grains are from CS4 (left), 15S2D (middle) and 15S2B (right) thin sections. Grains locations are indicated in Fig.5 with black boxes labelled as a^1, b^2 and c^2. These show the respective grain location within each thin section respectively.

same vertical extent but freely variable remanent magnetization intensities and directions; the model gave a RMS error to the observed anomaly of 8.9. In the last model M3 the modeled grain is subdivided in multiple tabular bodies, each one homogeneously magnetized, which are inverted to obtain the best fit between the observed and the calculated anomaly. The model M3 gave a RMS error of 3 and similar to the grain in CS4 suggests multiple sources of magnetization within the larger grains with higher intensities on the right side of the grain. This can be explained by variations in the amount of magnetite versus pentlandite. The stereo plot in Fig. 11 shows the magnetization direction of each sub-grain, which indicates extremely variable magnetization within the composite particle.

Two grains from the serpentinized thin section 15S2B were modeled (Fig. 12). The opaque grains are magnetite intergrown with pentlandite, pyrrhotite, and minor chalcopyrite. Two tests were performed: the first test assumes the two grains are homogeneously magnetized, and that the two larger grains are the main source of the observed anomalies. The second test (analogously to the M3 in the previous modeled grains) inverts a set of tabular bodies for remanent magnetization direction and intensity. The best fitting model in the first test gave a RMS error of 14 with a notable mismatch on the right side of the modeled area. This test suggests that an important source of magnetization is located below the large grain to the right of the modeled area, which is reversely magnetized (black box in Fig. 12). In reflected light, at high magnification, smaller magnetite grains (up to 10 μm) are visible on the surface of the thin section, and additional particles are likely below the surface of the sample. This area has been modeled in the second test by mean of tabular bodies, which gave a localized NRM intensity of 12 A/m, and steep negative inclination and an improved RMS error of 5.

Modeling of the magnetic anomalies over the three isolated grains in the thin section indicates heterogeneous sources of remanent magnetization with intensities varying between 2 and 12 A/m and variable directions. In the CS4 sample this variability may be associated with a variable amount of small ferrichromite exsolved within the hosting Cr- spinel. In the two serpentinized thin sections generally weaker NRMs correlate with a larger amount of pentlandite versus magnetite. In these samples the magnetization was acquired when magnetite was produced during serpentinization at lower temperature than the blocking temperature. The variable direction of the NRMs may also reflect the multidomain behavior expected for such large grains, which results in a less efficient acquisition of the magnetization.

4. Discussion

We investigated three samples of the Reinfjord Ultramafic Complex using rock magnetic methods, optical and electron microscopy and magnetic modeling. The bulk susceptibility and NRM of the serpentinized and pristine dunite samples vary by more than one order of magnitude. These properties were investigated with respect to the magnetic mineralogy, composition, fabric and texture. Magnetic scans of thin sections were used to locate the magnetic sources that result in distinct magnetic anomalies. We have shown that the magnetic mineralogy, the source of the magnetic anomalies, is significantly different in the pristine and serpentinized dunite samples. In the pristine dunite sample, where the primary magnetic mineralogical assemblage is preserved, the predominant source is Cr-spinel with fine exsolution microstructures (1–3 μm) of iron-rich ferrichromite to end-member magnetite. The Cr-spinel host is paramagnetic at room temperature due to its composition, therefore the exsolution intergrowths are the source of the magnetic anomalies. Thermomagnetic experiments confirm that there is a compositional variation within the grains which is reflected in the wide Tc temperature range between 200 °C and 579 °C (Table 3). The Verwey transition in the temperature versus susceptibility curves indicates the presence of near end-member magnetite. By contrast the predominant magnetic carrier in the serpentinized samples is end-member magnetite. Hysteresis parameters on the CS4 sample

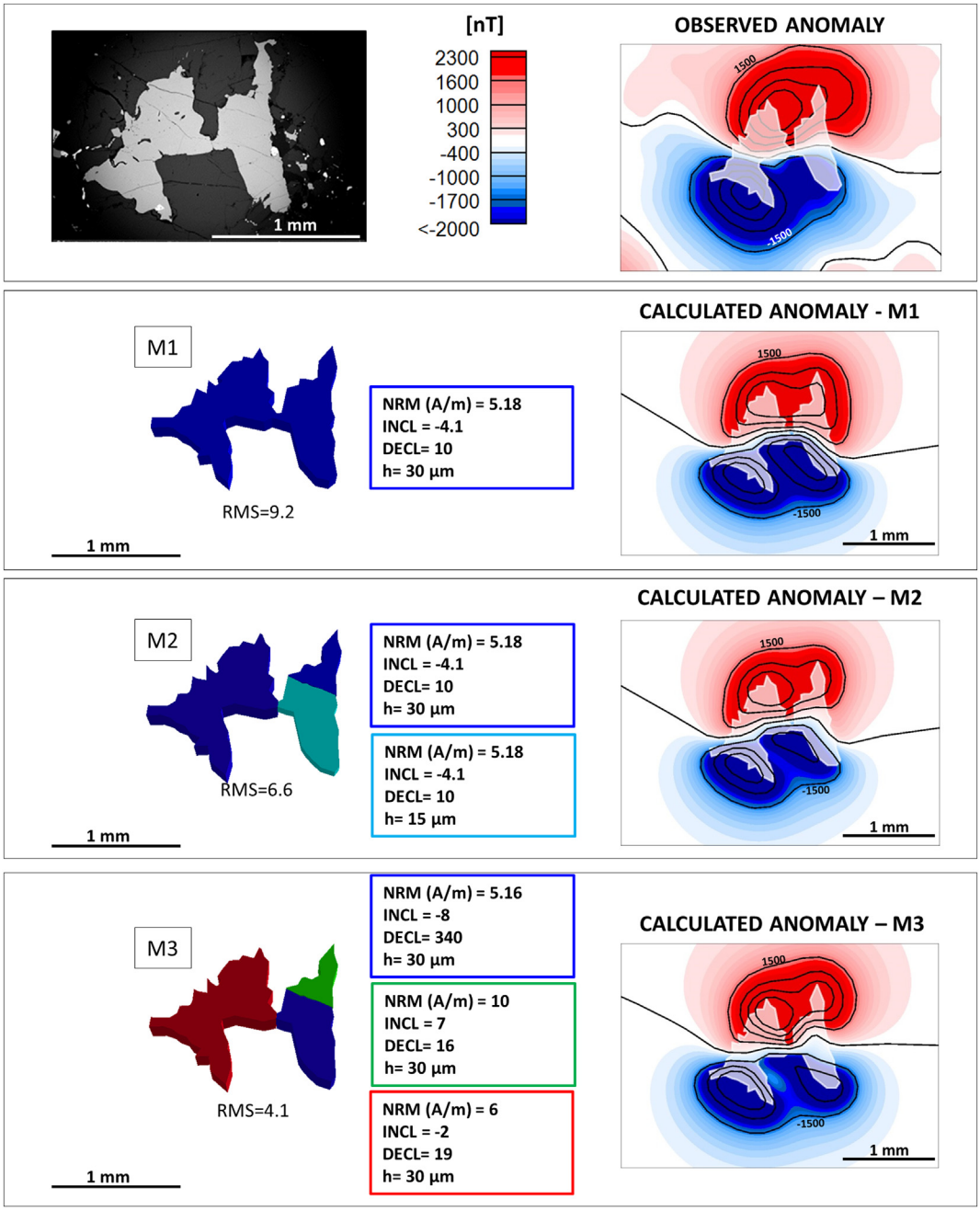

Fig. 10. NRM modeling tests for CS4 grain. Top panel: SEM image of the modeled Cr-spinel grain and correlative magnetic anomaly. Below for each test are: 3D image of the grain color coded by number of bodies used in the modeling (left) and respective modeling parameters (center) and resulting calculated anomaly (right) with contours interval of 1500 nT. RMS = root means square error between calculated and observed anomaly grids.

indicates that the bulk signal is a mixture of pseudo-single domain and single-domain size grains with relatively high coercivity, which can be explained by the presence of fine exsolution blebs. These are not homogeneously distributed within the Cr-spinel grains and likely the cause of the heterogeneous sources of magnetization shown in the analytic signal map and in the modeling results. Our modeling results confirm the microscopic observation of stronger magnetic intensity in areas of greater occurrences of ferrichromite exsolution within the Cr-rich spinel and weaker intensity where these exsolved phases were not observed.

In the serpentinized dunite thin sections, the largest anomalies correlate with larger grains of magnetite commonly found together with pentlandite or other sulfides. Thermal experiments indicate magnetite is the main magnetic carrier in the sample. Characteristic features which indicate magnetite, are the well-defined Hopkinson peaks and Verwey transitions, observed in the temperature-susceptibility curves, and the Tc estimates close to the Tc of endmember magnetite. The magnetite in veins, observed at the SEM, is fine grained, in agreement with the hysteresis parameters (Mr/Ms and Hcr/Hc) approaching values that are diagnostic of very fine single-domain particles. Most of the fine magnetite grains have a relatively small effect on the observed magnetic scans' anomalies. This is possibly related to the resolution of the magnetic scans; lowering the sensor height and increasing the sampling density could better resolve the sources of the magnetization but this has instrumental challenges. It is also possible that, although the field intensity is weaker on the magnetic scan, the sources of these anomalies may contribute to the bulk properties if they preserve a consistent magnetization direction throughout the sample. Here, we

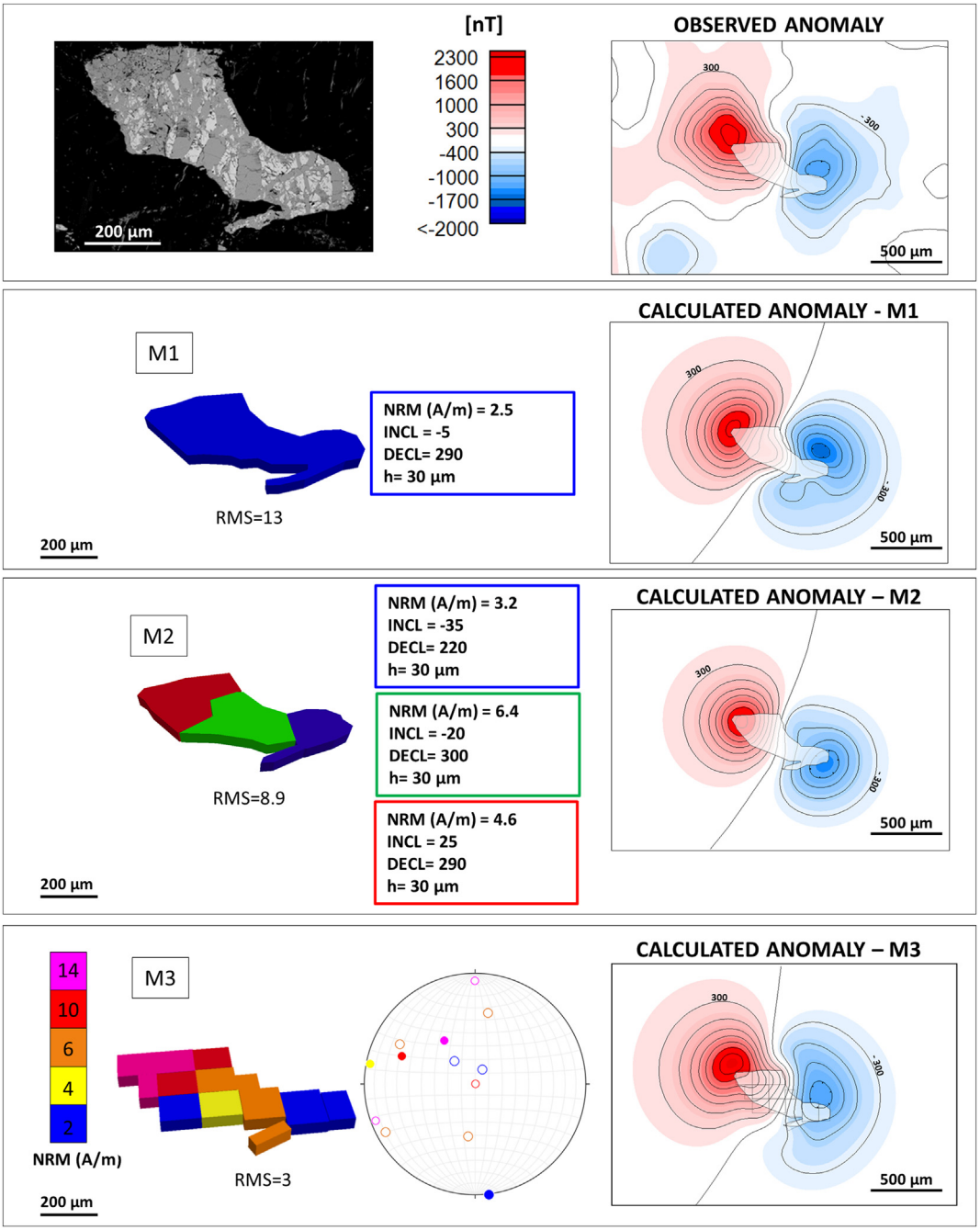

Fig. 11. NRM modeling test results for 15S2D grain. Top an SEM image of the modeled grain. For each test there is a panel with 3D image of the grain color coded by number of bodies used in the modeling (left) and respective modeling parameters (center) and resulting calculated anomaly (right) with contours interval of 300 nT. RMS = root means square error between calculated and observed anomaly grids. The stereo plot in the M3 model is for NRM directions of the modeled tabular bodies; closed circles are for positive inclinations and open circles for negative inclinations, colors are for NRMs intensities.

modeled only the anomalies caused by larger grains that are associated with the highest field intensities. Most of the fine-grained magnetite in the serpentinized samples formed during serpentinization and, as suggested by the ratio between NRM and Mr (Table 2), yields a lower efficiency of magnetization with respect to the magnetic carriers in the pristine dunite sample. The Cr-spinel in the dunite likely developed the magnetic Fe-rich exolution microstructures when cooling through the solvus at temperatures near, or above their respective Tc, therefore the NRM in this sample can be considered a thermoremanent magnetization (TRM). For non-interactingsingle-domain particles, Stacey and Banerjee (1974) calculate that remanence acquired during growth through chemical alteration (e.g. during serpentinization), a chemical remanent magnetization (CRM), must be smaller than the TRM of the same particles. While a similar calculation cannot be made for grains with other domain states, which are common in natural samples, Smirnov and Tarduno (2005) argue that the CRM of particles with other domain states is likely to be even weaker than those that are single-domain. This suggests that magnetization acquired during serpentinization (here <400 °C) must have a lower efficiency than a TRM, consistent with our observations on the efficiency of pristine dunite and serpentinite samples.

Modeling of the large discrete magnetic grains in the serpentinized samples confirms the microscopic observation of stronger magnetic intensity in areas of discrete magnetite, and weaker intensity where magnetite is found together with pentlandite, or other sulfides (chalcopyrite and pyrrhotite). The orientation of the magnetic anomalies varies across

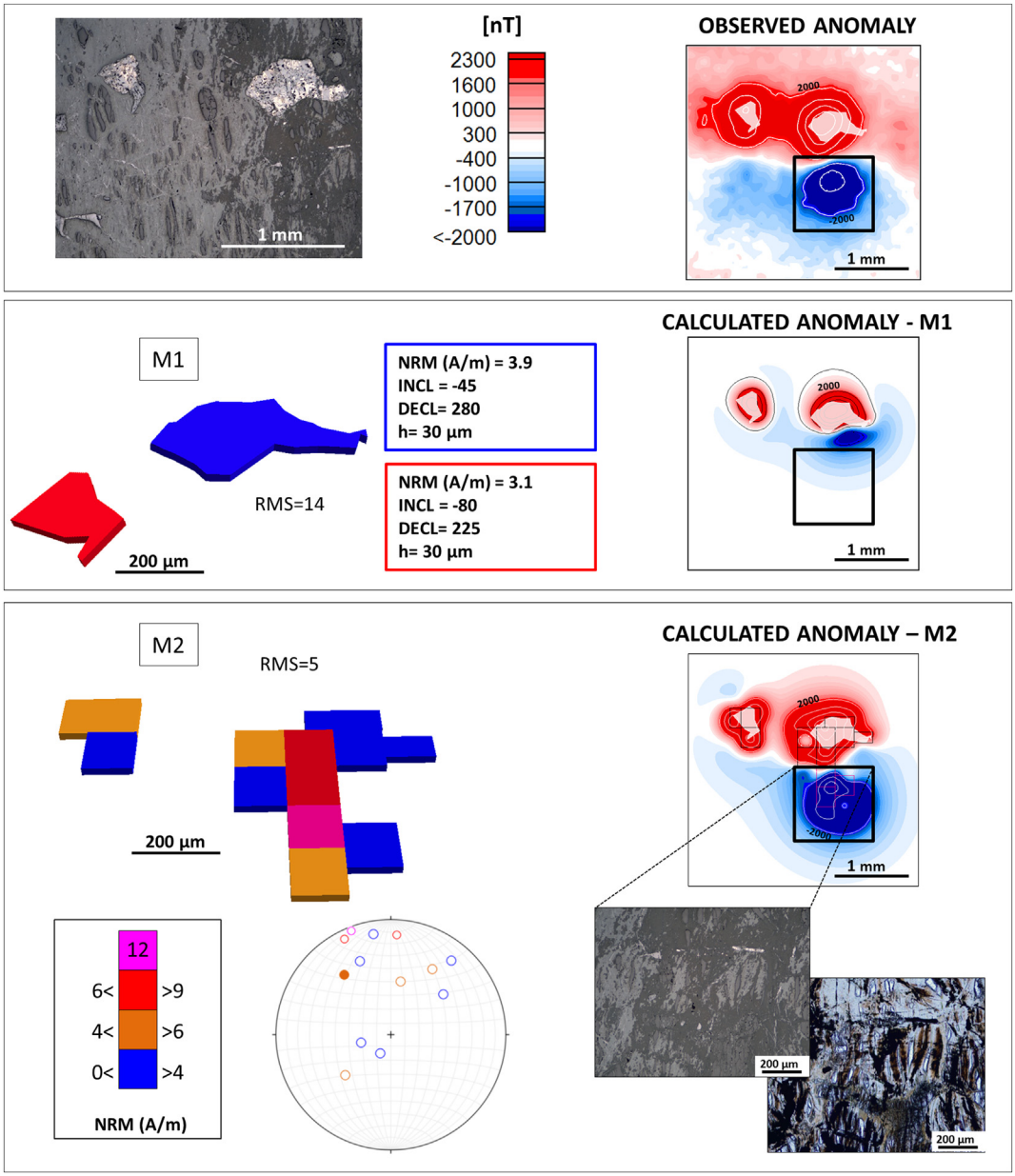

Fig. 12. NRM modeling tests for 15S2B grain. Above are reflected light image of the modeled grains and measured anomaly. Below (for each test) are: 3D image of the grain color coded by number of bodies used in the modeling (left) and respective modeling parameters (center) and resulting calculated anomaly (right) with contours interval of 2000 nT. RMS = root means square error between calculated and observed anomaly grids. The stereoplot in the M2 model is for NRM directions of the modeled tabular bodies; closed circles are for positive inclinations and open circles for negative inclinations, circles' colors indicate NRM intensities.

these thin sections and in future work this variation could be tied to the magnetic history, or the stability of NRM and acquisition of recent magnetic components. Such lines of enquiry could provide information on the timing of the serpentinization reactions. Scanning magnetic microscopy could be used to distinguish between primary and later magnetite formed during serpentinization, by measuring the magnetization of individual, or assemblages of grains.

To summarize, modeling of the magnetic anomalies over isolated grains indicated heterogeneous sources of NRM within the grains in serpentinite with intensities varying from 2 to 14 A/m and variable directions. These estimates are slightly higher for the serpentinized sample grains than in the pristine dunite. This result together with the composition, the percentage of magnetic minerals and the fine-grain size of the magnetic material in the serpentinized sample explain its high bulk magnetic susceptibility and NRM.

5. Conclusions

Scanning magnetic microscopy was used here to map the magnetic mineralogy of serpentinized and pristine dunite samples. Magnetic modeling in combination with chemical and magnetic properties analyses allowed characterization of the main magnetic carriers. The main results are summarized below:

- Magnetic carriers were identified based on Curie temperatures estimates and microscopic observations. In the serpentinized samples the magnetic carriers are end-member magnetite found both in veins, and as discrete large grains. Minor pyrrhotite was also observed. In the pristine dunite sample, the magnetic carriers are exsolution blebs with ferrichromite to end-member magnetite compositions in the Cr-spinel grains.

- The bulk NRM and magnetic susceptibility values are one order magnitude lower in the dunite sample than the serpentinized samples. This is explained by differences in magnetic mineralogy, content, grain size and texture between the serpentinized and the dunite samples. In the dunite sample the percentage of magnetic minerals calculated from Ms values is approximately 0.2%. Here, ferrichromite and minor magnetite exsolution microstructures in the Cr-spinel contribute to the magnetization. In the serpentinized sample the percentage of magnetic oxides is significantly larger at 2.8%, as calculated from Ms. Hysteresis properties indicate that the magnetite grains range from single domain to pseudo-single domain in size.
- Detailed modeling of a magnetic anomaly over an isolated grain indicates that there are heterogeneous sources of magnetic direction and intensity within the grain, in both pristine and serpentinized dunite samples.
- In the pristine dunite sample the heterogeneity is limited to the magnetization intensity which we interpret to be caused by variable concentration and composition of the ferrichromite exsolution within the Cr-spinel. However, the direction of magnetization is similar throughout the grain, implying similar timing of acquisition of magnetization for the exsolution microstructures.
- In the anomaly modeled over the serpentinized sample this heterogeneity applies both to the intensity and direction of the magnetization.
- Evaluating a larger view of the magnetic scan of the pristine dunite sample shows dipolar anomalies of similar orientation across the entire thin section. This suggests a consistent magnetization direction and may imply that the bulk magnetization direction of the sample is consistent with the fine-scale magnetization mapped here, and that this was acquired during initial cooling through the magnetite – Cr-spinel solvus, after emplacement. In the serpentinized samples the scans show variability in the orientation of the large dipolar anomalies among the different magnetite grains in the thin section. This heterogeneity will lower the total NRM. However, the fine-grained magnetite located in the veins will also add to the NRM. Future work would include demagnetization of the thin sections followed by magnetic mapping. This could be used to investigate the stability of the magnetization, and to explain better the non-unidirectional magnetization in the serpentinized samples.

We conclude that the bulk magnetic properties of these samples can be explained by the observed magnetic mineralogy. Forward modeling was effective in defining areas of higher magnetization that was constrained by the 3D geometry of the magnetic grains. Serpentinization clearly affected the heterogeneity of the magnetization direction across the thin section. The observation of numerous anomalies with variable directions and intensities over the larger grains in the magnetic scans of the serpentinites may suggest that the magnetization was acquired over a long time interval. In order to investigate further the link between the bulk NRM and the magnetization of the discrete grains, modeling of the entire thin section should be made. Curvature analysis (Phillips et al., 2007) of the magnetic data acquired by scanning magnetic microscopy could be used to automatically determine the boundaries of magnetic sources across the entire thin section. This is planned for future work.

Acknowledgments

We thank the editors Bjørn Jamtveit and Marguerite Godard, and the two anonymous reviewers in addition to Peter Robinson, Alexander Michels, Richard Blakely and Hajo Götze for constructive comments. The research leading to these results was funded by People Programme (Marie Curie Actions) of the European Union's Seventh Framework ProgrammeFP7/2007-2013/underREA– Grant Agreement n° 608001. The Research Council of Norway is acknowledged for the support to the Norwegian Micro- and Nano-Fabrication Facility, NorFab, project number 245963/F50, and development of the scanning magnetic microscope (NFR grant 222666). Scanning SQUID microscopy was conducted during the visit of S.A. McEnroe to GSJ/AIST supported by JSPS invitation fellowship (S16128). Ayako Katayama is thanked for the help in measurement of scanning SQUID microscopy. We further thank Andrea Risplendente for his technical assistance at the microprobe.

Appendix A. Supplementary data

Supplementary data to this article can be found online at https://doi.org/10.1016/j.lithos.2018.09.018.

References

Barnes, S.J., Roeder, P.L., 2001. The range of spinel compositions in terrestrial mafic and ultramafic rocks. J. Petrol. 42, 2279–2302.
Church, N., McEnroe, S., 2018. Magnetic Field Surveys of Thin Sections. https://doi.org/10.1071/ASEG2018abW10_3F.
Clark, D.A., 1997. Magnetic petrophysics and magnetic petrology: aids to geological interpretation of magnetic surveys. AGSO J. Aust. Geol. Geophys. 17, 83–104.
Day, R., Fuller, M., Schmidt, V., 1977. Hysteresis properties of titanomagnetites: grain-size and compositional dependence. Phys. Earth Planet. Inter. 13, 260–267.
Domenichini, B., Amilain-Basset, K., Bourgeois, S., 2002. Dynamic segregation during ferrite oxidation revealed by XPS. Surf. Interface Anal. 34, 527–530.
Dunlop, D.J., 2002. Theory and application of the Day plot (Mrs/Ms versus Hcr/Hc) 1. Theoreticalcurves and tests using titanomagnetite data. J. Geophys. Res. Solid Earth 107.
Dunlop, D.J., Özdemir, Ö., 1997. Rock Magnetism: Fundamentals and Frontiers. Cambridge University Press.
Fabian, K., Shcherbakov, V.P., McEnroe, S.A., 2013. Measuring the Curie temperature. Geochem. Geophys. Geosyst. 14, 947–961.
Francombe, M., 1957. Lattice changes in spinel-type iron chromites. J. Phys. Chem. Solids 3, 37–43.
Fu, R.R., Lima, E.A., Weiss, B.P., 2014. No nebular magnetization in the Allende CV carbonaceous chondrite. Earth Planet. Sci. Lett. 404 (C), 54–66. https://doi.org/10.1016/j.epsl.2014.07.014.
Fukuzawa, T., Nakamura, N., Oda, H., Uehara, M., Nagahama, H., 2017. Generation of billow-like wavy folds by fluidization at high temperature in Nojima fault gouge: microscopic and rock magnetic perspectives. Earth Planets Space 69, 54.
Funaki, M., Tunyi, I., Orlický, O., Porubcan, V., 2000. Natural remanent magnetization of Rumanova chondrite (H5) acquired by the shock metamorphisms S3. Antarctic Meteor. Res. 13, 78.
Grannes, K.R.B., 2016. Cryptic Variations of Olivene and Clinopyroxene in the RF-4Drill-Core:- A Geochemical Study of the Reinfjord Ultramafic Complex, Norway. NTNU.
Hankard, F., Gattacceca, J.m., Fermon, C., Pannetier-Lecoeur, M., Langlais, B., Quesnel, Y., Rochette, P., McEnroe, S.A., 2009. Magnetic field microscopy of rock samples using a giant magnetoresistance–based scanning magnetometer. Geochem. Geophys. Geosyst. 10.
Harrison, R.J., Putnis, A., 1996. Magnetic Properties of the Magnetite-Spinel Solid Solution: Curie Temperatures, Magnetic Susceptibilities, and Cation Ordering. Mineralogical Society of America.
Horen, H., Soubrand, M., Kierczak, J., Joussein, E., Néel, C., 2014. Magnetic characterization of ferrichromite in soils developed on serpentinites under temperate climate. Geoderma 235, 83–89.
Kądziałko-Hofmokl, M., Delura, K., Bylina, P., Jeleńska, M., Kruczyk, J., 2008. Mineralogy and magnetism of Fe-Cr spinel series minerals from podiform chromitites and dunites from Tapadla (Sudetic ophiolite, SWPoland) and their relationship to palaeomagnetic results of the dunites. Geophys. J. Int. 175, 885–900.
Kawai, J., Oda, H., Fujihira, J., Miyamoto, M., Miyagi, I., Sato, M., 2016. SQUID microscope with hollow-structured cryostat for magnetic field imaging of room temperature samples. IEEE Trans. Appl. Supercond. 26, 1–5.
Larsen, R.B., Grant, T., Sørensen, B.E., Tegner, C., McEnroe, S., Pastore, Z., Fichler, C., Nikolaisen, E., Grannes, K.R., Church, N., 2018. Portrait of a giant deep-seated magmatic conduit system: the Seiland Igneous Province. Lithos 296, 600–622.
Lima, E.A., Bruno, A.C., Carvalho, H.R., Weiss, B.P., 2014. Scanning magnetic tunnel junction microscope for high-resolution imaging of remanent magnetization fields. Meas. Sci. Technol. 25, 105401.
McEnroe, S.A., Brown, L.L., Robinson, P., 2009a. Remanent and induced magnetic anomalies over a layered intrusion: effects from crystal fractionation and magma recharge. Tectonophysics 478, 119–134.
McEnroe, S.A., Fabian, K., Robinson, P., Gaina, C., Brown, L.L., 2009b. Crustal magnetism, lamellar magnetism and rocks that remember. Elements 5, 241–246.
McEnroe, S.A., Robinson, P., Miyajima, N., Fabian, K., Dyar, D., Sklute, E., 2016. Lamellar magnetism and exchange bias in billion-year-old titanohematite with nanoscale ilmenite exsolution lamellae: I. Mineral and magnetic characterization. Geophys. J. Int. 206, 470–486.
McEnroe, S.A., Robinson, P., Church, N., Purucker, M., 2018. Magnetism at depth: a view from an ancient continental subduction and collision zone. Geochem. Geophys. Geosyst. 19, 1123–1147.

Minyuk, P., Subbotnikova, T., Brown, L., Murdock, K., 2013. High-temperature thermomagnetic properties of vivianite nodules, Lake El'gygytgyn, Northeast Russia. Clim. Past 9, 433.

Nabighian, M.N., 1972. The analytic signal of two-dimensional magnetic bodies with polygonal cross-section: its properties and use for automated anomaly interpretation. Geophysics 37, 507–517.

Noguchi, A., Oda, H., Yamamoto, Y., Usui, A., Sato, M., Kawai, J., 2017. Scanning SQUID microscopy of a ferromanganese crust from the northwestern Pacific: sub-millimeter scale magnetostratigraphy as a new tool for age determination and mapping of environmental magnetic parameters. Geophys. Res. Lett. 44, 5360–5367.

Oda, H., Usui, A., Miyagi, I., Joshima, M., Weiss, B.P., Shantz, C., Fong, L.E., McBride, K.K., Harder, R., Baudenbacher, F.J., 2011. Ultrafine-scale magnetostratigraphy of marine ferromanganese crust. Geology 39, 227–230.

Oda, H., Kawai, J., Miyamoto, M., Miyagi, I., Sato, M., Noguchi, A., Yamamoto, Y., Fujihira, J.-i., Natsuhara, N., Aramaki, Y., 2016. Scanning SQUID microscope system for geological samples: system integration and initial evaluation. Earth Planets Space 68, 179.

Petersen, N., Bleil, U., 1982. 6.2.5 Curie temperature: datasheet from Landolt-Börnstein – Group V Geophysics. In: Angenheister, G. (Ed.), "Subvolume B" in Springer Materials. Vol. 1B. Springer-Verlag, Berlin, Heidelberg. https://doi.org/10.1007/10201909_76.

Phillips, J.D., Hansen, R.O., Blakely, R.J., 2007. The use of curvature in potential-field interpretation. Explor. Geophys. 38, 111–119.

Puranen, R., 1989. Susceptibilities, Iron and Magnetite Content of Precambrian Rocks in Finland. 90th ed. Geological Survey of Finland, Report of Investigation.

Readman, P., O'Reilly, W., 1972. Magnetic properties of oxidized (cation-deficient) titanomagnetites (Fe, Ti, block) 304. J. Geomagnet. Geoelect. 24 (1), 69 &. (O'Reilly did a huge amount of work on effect of oxidation state).

Robbins, M., Wertheim, G., Sherwood, R., Buchanan, D., 1971. Magnetic properties and site distributions in the system FeCr2O4-Fe3O4 (Fe2+ Cr2− xFex3+ O4). J. Phys. Chem. Solids 32, 717–729.

Robinson, P., McEnroe, S., Miyajima, N., Fabian, K., Church, N., 2016. Remanent magnetization, magnetic coupling, and interface ionic configurations of intergrown rhombohedral and cubic Fe-Ti oxides: a short survey. Am. Mineral. 101, 518–530.

Roest, W.E., Verhoef, J., Pilkington, M., 1992. Magnetic interpretation using 3-D analytic signal. Geophysics 57, 116–125.

Smirnov, A.V., Tarduno, J.A., 2005. Thermochemical remanent magnetization in Precambrian rocks: are we sure the geomagnetic field was weak? 110 (B6), B06103. https://doi.org/10.1029/2004JB003445.

Stacey, F.D., Banerjee, S.K., 1974. The Physical Principles of Rock Magnetism. Elsevier Scientific Publishing Company.

Tauxe, L., 1998. Paleomagnetic Principles and Practice. Kluwer, New York.

Thomas, I.M., Moyer, T.C., Wikswo Jr., J.P., 1992. High resolution magnetic susceptibility imaging of geological thin sections: pilot study of a pyroclastic sample from the Bishop Tuff, California, U. S.A, Geophys Res Lett 19 (21), 2139–2142. https://doi.org/10.1029/92GL02322.

Tominaga, M., Beinlich, A., Lima, E.A., Tivey, M.A., Hampton, B.A., Weiss, B., Harigane, Y., 2017. Multi-scale magnetic mapping of serpentinite carbonation. Nat. Commun. 8, 1870.

Walz, F., 2002. The Verwey transition – a topical review. J. Phys.- Condens. Mat. 14 (12), R285–R340. https://doi.org/10.1088/0953-8984/14/12/203.

Weiss, B.P., Kirschvink, J.L., Baudenbacher, F.J., Vali, H., Peters, N.T., Macdonald, F.A., Wikswo, J.P., 2000. A low temperature transfer of ALH84001 from Mars to Earth. Science 290, 791–795.

Weiss, B.P., Lima, E.A., Fong, L.E., Baudenbacher, F.J., 2007. Paleomagnetic analysis using SQUID microscopy. J. Geophys. Res. Solid Earth 112.

Weiss, B.P., Fong, L.E., Vali, H., Lima, E.A., Baudenbacher, F.J., 2008. Paleointensity of the ancient Martian magnetic field. Geophys. Res. Lett. 35 (23), L23207. https://doi.org/10.1029/2008GL035585 (2008).

Weiss, B.P., Vali, H., Baudenbacher, F.J., Kirschvink, J.L., Stewart, S.T., Shuster, D.L., 2002. Records of an ancient Martian magnetic field in ALH84001. Earth Planet. Sci. Lett. 201, 449–463.